

Morphology of retrogressive failures in the Eastern Rhone interfluvе during the last glacial maximum (Gulf of Lions, Western Mediterranean)

Shray Badhani ^{a,b,*}, Antonio Cattaneo ^a, Bernard Dennielou ^a, Estelle Leroux ^a, Florent Colin ^{a,b}, Yannick Thomas ^a, Gwenael Jouet ^a, Marina Rabineau ^b, Laurence Droz ^b

^a IFREMER, Unité de Recherche Géosciences Marines, Centre de Bretagne, 1625 Route de Sainte-Anne, 29280, Plouzané, France

^b Univ. Brest, CNRS, Univ. Bretagne-Sud, Laboratoire Géosciences Océan, UMR6538 - IUEM, rue Dumont d'Urville, F-29280, Plouzané, France



ARTICLE INFO

Article history:

Received 28 May 2019

Received in revised form 1 October 2019

Accepted 2 October 2019

Available online 15 November 2019

Keywords:

Submarine landslide

Mass transport deposits

Gulf of Lions

Western Mediterranean

Turbiditic levees

ABSTRACT

The Gulf of Lions (NW Mediterranean Sea) is a SW-NE oriented passive continental margin formed since the Oligocene. It presents small to large scale mass movement features suggesting a long history of seafloor instability. Of particular interest are the two surficial large mass-transport deposits along the Rhone turbiditic levee, known as the Rhone Eastern and Western Mass-Transport Deposits (REMTD and RWMTD). With the help of the recently acquired multi-beam bathymetric, sub-bottom profiler, high-resolution seismic and sedimentological data, we investigate the morphology, timing, kinematics, and possible triggering mechanisms of the source area of the REMTD, which we refer to as the Eastern Rhone Interfluvе Slide (ERIS). ERIS has an estimated run-out distance of approximately 200 km. It covers an area of about 700 km² and the volume of the mobilized material is approximately 110 km³. Our data reveal four individual glide planes within the ERIS complex which were most likely generated by retrogressive failures. The basal surfaces of the ERIS coincide with high-amplitude seismic reflectors similar to those previously interpreted as the expression of condensed sections on the upper slope. The turbiditic sequences sandwiched between the condensed sections likely control the localisation of potential weak layers favouring the failures. AMS radiocarbon dating yields an age of approximately 21 ka cal BP for the failures, which falls within the peak of the Last Glacial Maximum. The toe area of the ERIS is incised by several active listric faults rooted in the Messinian strata, which control the location of the slide scarps. The combination of several factors such as slope steepening, halokinesis, and excess pore pressure generation due to rapid turbiditic sedimentation during the Last Glacial Maximum are considered as the possible candidates for the triggering of the failures in the investigated slope.

© 2019 The Authors. Published by Elsevier B.V. This is an open access article under the CC BY-NC-ND license (<http://creativecommons.org/licenses/by-nc-nd/4.0/>).

1. Introduction

Submarine landslides are one of the widespread phenomena known to shape the continental margins (Posamentier and Kolla, 2003). They redistribute large volumes of sediment from the shelf or the upper slopes to the lower slope or deep basin. Furthermore, they can be far larger than any terrestrial landslide and threaten offshore infrastructure. Most importantly, they pose a risk to increasingly populated coastlines by triggering devastating tsunamis (Bryant et al., 2005, 2003; Kvalstad et al., 2005; Tappin et al.,

1999). The most recent example of a submarine landslide triggered tsunami came to public attention when an earthquake of magnitude Mw 7.5 most likely caused a submarine landslide off Sulawesi, Indonesia. This resulted in a tsunami with a wave height of about seven metres, killing more than 4000 people and displacing about 200,000 inhabitants (Carvajal et al., 2019; Heidarzadeh et al., 2018; Sassa and Takagawa, 2019).

Submarine landslides can disintegrate and transport a large amount of slope-forming sediments, where the shear failure occurs along one or several planes (Eckel, 1958; Hampton et al., 1996; Schuster and Krizek, 1978). Due to their locations in deepwater settings, direct observation of submarine landslides and their deposits is difficult. Therefore, geophysical techniques namely multibeam bathymetry, reflection seismic are used to investigate submarine landslides. In reflection seismic data submarine landslide deposits

* Corresponding author at: IFREMER, Unité de Recherche Géosciences Marines, Centre de Bretagne, 1625 Route de Sainte-Anne, 29280, Plouzané, France.

E-mail address: shray.badhani@ifremer.fr (S. Badhani).

are generally referred to as mass transport deposits (MTDs) and mass transport complexes (Alves, 2015; Frey Martinez et al., 2005). MTDs usually cover areas exceeding thousands of square kilometres and have volumes in hundreds of cubic kilometres, depositing slide material hundreds of kilometres from their source areas, on the continental shelf or upper slope, onto the deep oceans (Bull et al., 2009; Frey Martinez et al., 2005; Gee et al., 2006; Masson et al., 2006; McAdoo et al., 2000; Shipp et al., 2004; Solow et al., 2009). In spite of the large sizes and volumes of sediments involved in the failure events, their link with local or global forcing is still a matter of debate (Hampton et al., 1996; Hühnerbach and Masson, 2004; Lee, 2009; Pope et al., 2015; Solow et al., 2009; Sultan et al., 2004; ten Brink et al., 2009; Urgeles and Camerlenghi, 2013; Urlaub et al., 2013). However, various authors (e.g. Locat and Lee, 2002 and references therein; Sultan et al., 2004; Vanneste et al., 2013) suggest that their occurrence is commonly controlled by one or a combination of favourable preconditioning factors and trigger mechanisms such as slope over-steepening, earthquakes, storm-wave loading, rapid sediment accumulation and under-consolidation, gas charging, gas hydrate dissociation, low tides, glacial loading, and volcanic island processes.

The Gulf of Lions (GoL) presents two large surficial MTDs with volumes exceeding 100 km³. These MTDs have been called by several names in previous studies, such as "Eastern and Western Debris Flows" (Bonnel et al., 2005; Droz et al., 2001; Lastras, 2007) or "Eastern and Western MTDs" (Droz et al., 2006), or more recently "Rhone Eastern Mass-Transport Deposit (REMTD)" and "the Rhone Western Mass-transport Deposit (RWMTD)" (Dennielou et al., 2019). To allow an easy correlation and comparison between the two studies, we follow the nomenclature of Dennielou et al. (2019).

The REMTD and RWMTD have previously been mapped and described in detail (Dennielou et al., 2019; Droz et al., 2006; Droz and Bellaiche, 1985); however, due to the lack of high-resolution data on the upper continental slope of the GoL margin, little attention has been paid to the source of the REMTD. This study therefore focuses on analyzing and characterizing the source area of the REMTD, which we hereafter refer to as the "Eastern Rhone Interfluvial Slide (ERIS)". The ERIS and REMTD together form the Eastern Rhone Interfluvial Slide Complex (ERISC). We present for the first time a detailed mapping of the ERISC with the combination of high-resolution multibeam bathymetry, high-resolution multi-channel seismic, sub-bottom profiler, and newly acquired sediment core data from the ERISC. We aim to 1) identify the morphological and sedimentological characteristics of ERIS, 2) establish a chronological framework for the failed sedimentary units based on direct and indirect dating methods, 3) identify the presence of potential weak layers, and 4) identify possible trigger mechanisms responsible for the occurrence of the ERIS. The detailed mapping of the ERISC is complementary to the submarine landslide archive that currently exists for the Mediterranean region (e.g. Urgeles and Camerlenghi, 2013). Even if the collection of landslide parameters is not always conducive to fully understand the triggering mechanisms of seafloor instabilities (e.g., Hühnerbach and Masson, 2004), Clare et al. (2018) suggest that the widening of landslide database is a key to improve knowledge and an important contribution to tackle outstanding scientific questions on hazard mitigation, especially if the measured parameters are consistently acquired.

2. Geological setting

The Gulf of Lions (Fig. 1) is a SW-NE oriented, young passive continental margin that formed after the Oligocene time, with the rotation of Corso-Sardinian block, in a context of convergence between Africa and Europe (Le Pichon et al., 1971). Due to its limited lateral extent and easy accessibility, the GoL is one of the

best-studied passive margins in the world (Berné and Gorini, 2005; Séranne, 1999; Steckler and Watts, 1980). The margin is characterised by a wide continental shelf (~70 km) that was sub-aerially exposed during the Last Glacial Maximum (LGM) about 21 ka ago and offers a continuous sedimentary record drilled on the upper slope by the PROMESS boreholes (Bassetti et al., 2008, 2006; Berné et al., 2007; Jouet, 2007; Rabineau et al., 2005). Being a passive margin, earthquakes greater than four Mw have never been recorded in the GoL since records exist (Cara et al., 2015). The present-day shelf break of the GoL occurs at water depths ranging from 120 to 170 m. Fifteen submarine canyons feed the distal Rhone Sedimentary System and incise the GoL continental slope down to 1000 m water depth, the major one being the Petit Rhone Canyon (PRC), which is fed by alpine sediments through the largest river Rhone and its tributaries.

The sedimentary architecture of the GoL drastically changed during a major event known as the Messinian Salinity Crisis, when a major sea-level drop in the Mediterranean Sea resulted in a km-scale thick evaporite deposition in the deep basin (Hsu, 1973). After reflooding of the basin during the Zanclean (5.33 Ma; Lofi et al., 2003; Roveri et al., 2008), a prograding and aggrading sedimentary prism of up to 3 km thick developed along with a large subsidence (up to 250 m/Ma on the shelf, Dennielou et al., 2019; Leroux et al., 2014; Rabineau et al., 2006, 2014 and up to 500 m/Ma in the deep basin, Leroux et al., 2015; Rabineau et al., 2014) throughout the Plio-Quaternary time to form the present-day margin morphology (Dennielou et al., 2019; Leroux et al., 2014). Since then, the evolution of the deeper part of the GoL has mainly been controlled by syn-sedimentary salt tectonics and gravity-driven deformation of post-Plio-Quaternary strata tuned by relative sea-level fluctuations. The gravity-driven deformation above the salt layer, which forms a "décollement" surface, led to the development of extensional areas dominated by listric faults and grabens on the upper and lower slope (Fig. 1) and compressional areas in the deep basin driven by salt diapirs and domes (dos Reis et al., 2005).

The Pleistocene sedimentation in the GoL was mainly controlled by glacio-eustatic sea-level fluctuations related to the Milankovitch cyclicities (Bassetti et al., 2008; Torres et al., 1995; Rabineau et al., 2005, 1998; Tesson and Gensous, 1998). During a major Quaternary reorganization called the Mid-Pleistocene Transition, the dominant climate cyclicity changed from 40 ka to 100 ka in frequency (Droz and Bellaiche, 1985; Pena and Goldstein, 2014). These cycles were accompanied by a change in sea-level cycle amplitudes from 50 m to 100 m (Droz et al., 2006; Pena and Goldstein, 2014). After the Mid-Pleistocene, sedimentation in the GoL was mainly dominated by terrigenous deposition brought by the Alpine rivers (mainly Rhone) into the basin through turbiditic systems. In the Late Pleistocene, the evolution of the margin and canyons was driven by sea-level fluctuations with the development of thick forced-regressive sequences during sea-level falls bounded on the slope by condensed intervals deposited during highstands (Bassetti et al., 2006; Rabineau et al., 2006; Sierro et al., 2009). On the lower slope of the GoL, which is mainly fed by the PRC, sedimentation rates for the glacial and deglacial periods were documented in the order of 1–2 m/ka, while during the interglacial periods the sedimentation rates were in the range of 0.05 to 0.10 m/ka (Dennielou et al., 2019; Lombo Tombo et al., 2015; Sierro et al., 2009).

3. Material and methods

Multi-beam bathymetric data were collected in the GoL since 1997 during several oceanographic campaigns listed in Table 1. In this study, we used two bathymetric datasets: an EMODNET 115 m resolution grid (Fig. 1; www.emodnet-bathymetry.eu, 2018) and

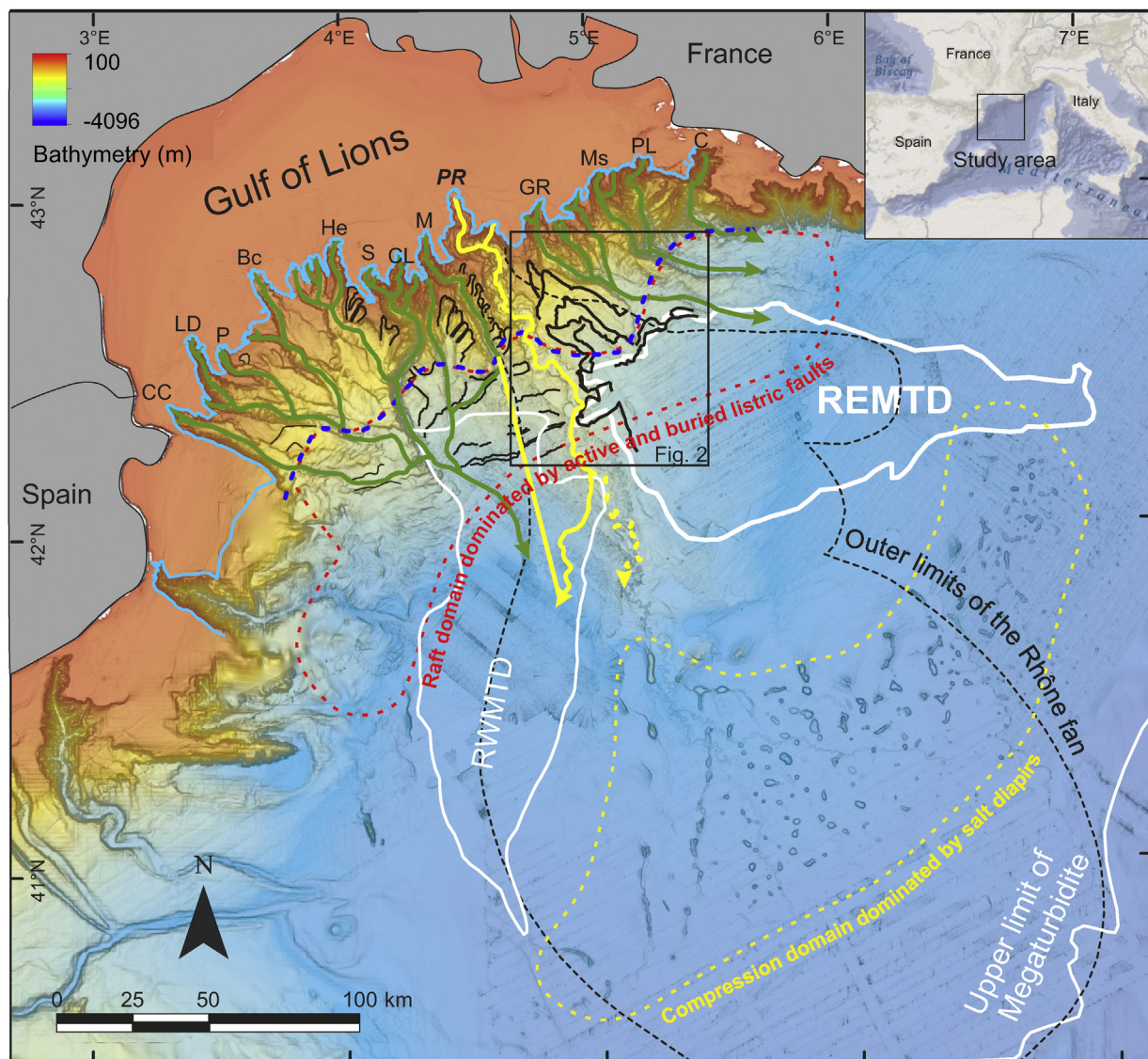


Fig. 1. EMODNET bathymetric map of Gulf of Lions margin highlighting the distribution of main sedimentary and mass movement features (black dashed lines: sedimentary deposits; white lines: Mass Transport Deposits; green lines: thalweg of main submarine canyons; blue line: shelf break; solid black line: headwall of submarine landslides; blue dashed line: upslope limit of Messinian evaporites; red dashed rounded polygon: raft domain dominated by listric faults; yellow dashed polygon: compression area dominated by salt diapirs). Gulf of Lions canyons (Berné et al., 2002): CC: Cap de Creus, LD: Lacaze Duthier, P: Pruvost, Bc: Bourcart, He: Herault, S: Sète, CL: Catherine Laurence, M: Marti, PR: Petit-Rhône, GR: Grand-Rhône, Ms: Marseille, PL: Planier, C: Cassidaigne. REMTD: Rhône Eastern Mass Transport Deposit, RWMTD: Rhône Western Mass Transport Deposit. Limits of sedimentary bodies are from Droz et al. (2006); Messinian evaporite limits are from dos Reis et al. (2005).

Table 1
Oceanographic campaigns and data used in this study.

Cruise	Year	Vessel	Data/attributes	Reference
PRISME2	2013	L'Atalante	EM122, 710, HR seismic, 3.5 kHz SBP	(Cattaneo, 2013b)
PRISME3	2013	Pourquoi pas?	3.5 kHz SBP, Calypso piston cores	(Cattaneo, 2013a)
AM-MED-1	2013	Le Suroit	EM300, HR seismic	(Rabineau et al., 2013)
SEEPGOL	2007	Le Suroit	EM300, 2–5.2 kHz SBP	(Rabineau and Aslanian, 2007)
PROGRESS	2003	Le Suroit	EM300, HR seismic, 2–5.2 kHz SBP	(Droz, 2003)
CALMAR97	1997	L'Atalante	EM12	(Loubrieu, 1997)
GMO1	2001	Le Suroit	EM300	(Cochonat, 2001)
GMO2-CARNAC	2002	Le Suroit	EM300	(Sultan and Voisset, 2002)
MARION	2000	Le Suroit	EM300	(Berné, 2000)
RHOSOS	2008	Le Suroit	EM300	(Berné and Dennielou, 2008)

recent 25–100 m resolution bathymetric grids (Figs. 2 a and 3 a, b) that were acquired using hull-mounted multibeam systems during the oceanographic campaigns listed in Table 1. The high-resolution bathymetric data were merged and gridded at a final grid size of 25 m using ArcMap 10.3 (www.arcgis.com).

High-resolution (HR) multi-channel seismic (MCS) reflection data used in this study were acquired using generator-injector (GI) source, analogue 24 channels streamer and 6.25 m trace spacing during PROGRES cruise (Droz, 2003) and a mini-GI source and digital 72 channels streamer with 6.25 m trace spacing during AM-

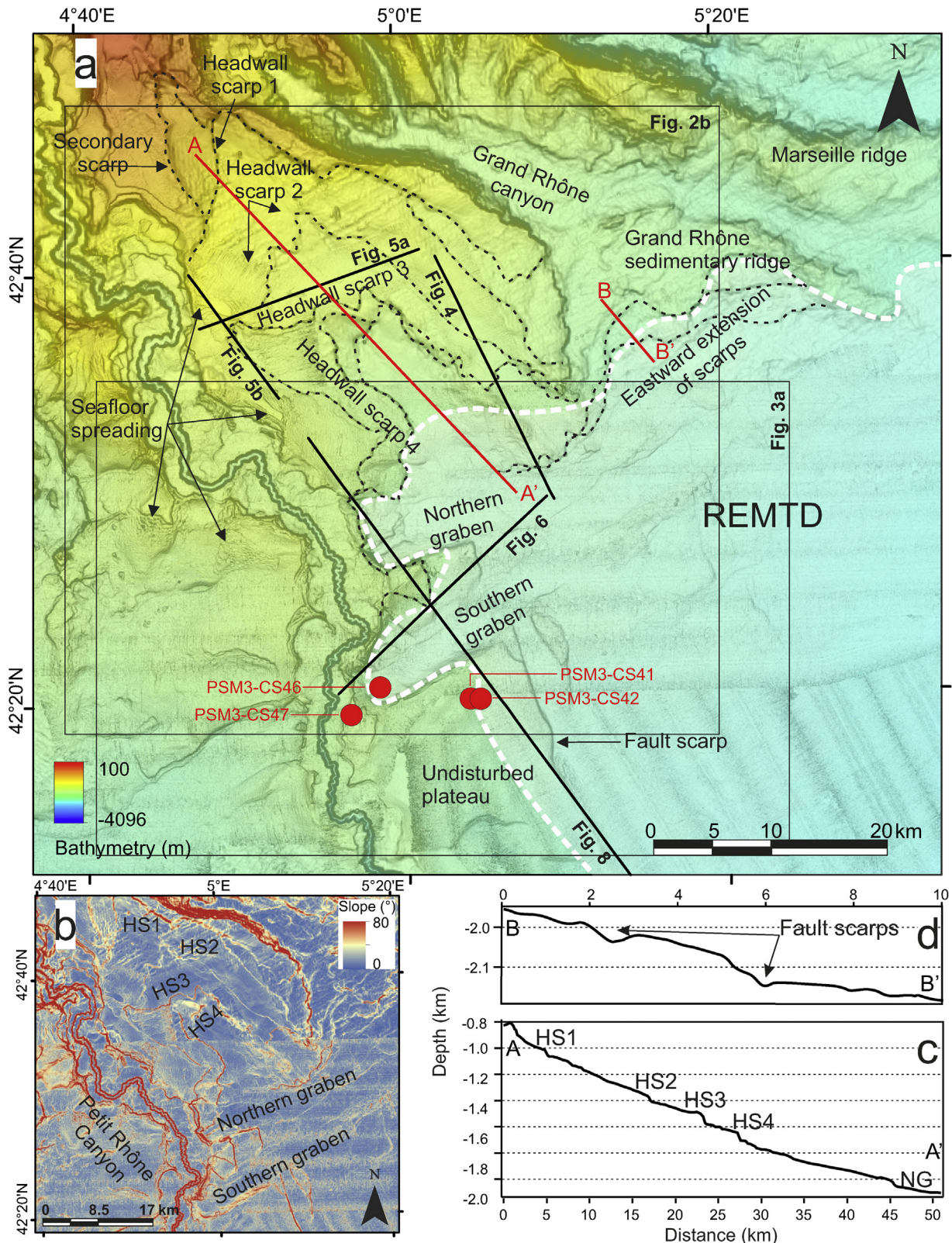


Fig. 2. a) High-resolution multibeam bathymetric map of the source area of the Eastern Rhône Interfluvial Slide Complex (ERISC) highlighting multiple retrogressive headwall scarps and associated sidewall scarps marked with dashed black lines. Red circles represent the locations of sediment cores acquired during PRISME3 cruise. Solid black lines represent locations of the seismic profiles shown in Figs. 3–5a, b and 7. Black rectangles represent locations and extent of Figs. 2b and 3a. b) Seafloor gradient map of the study area. c) Bathymetric profile A-A' illustrates the locations of four individual headwalls and the Northern Graben and d) Bathymetric profile B-B' shows morphologic expressions of the fault scarps towards the eastern part of the study area.

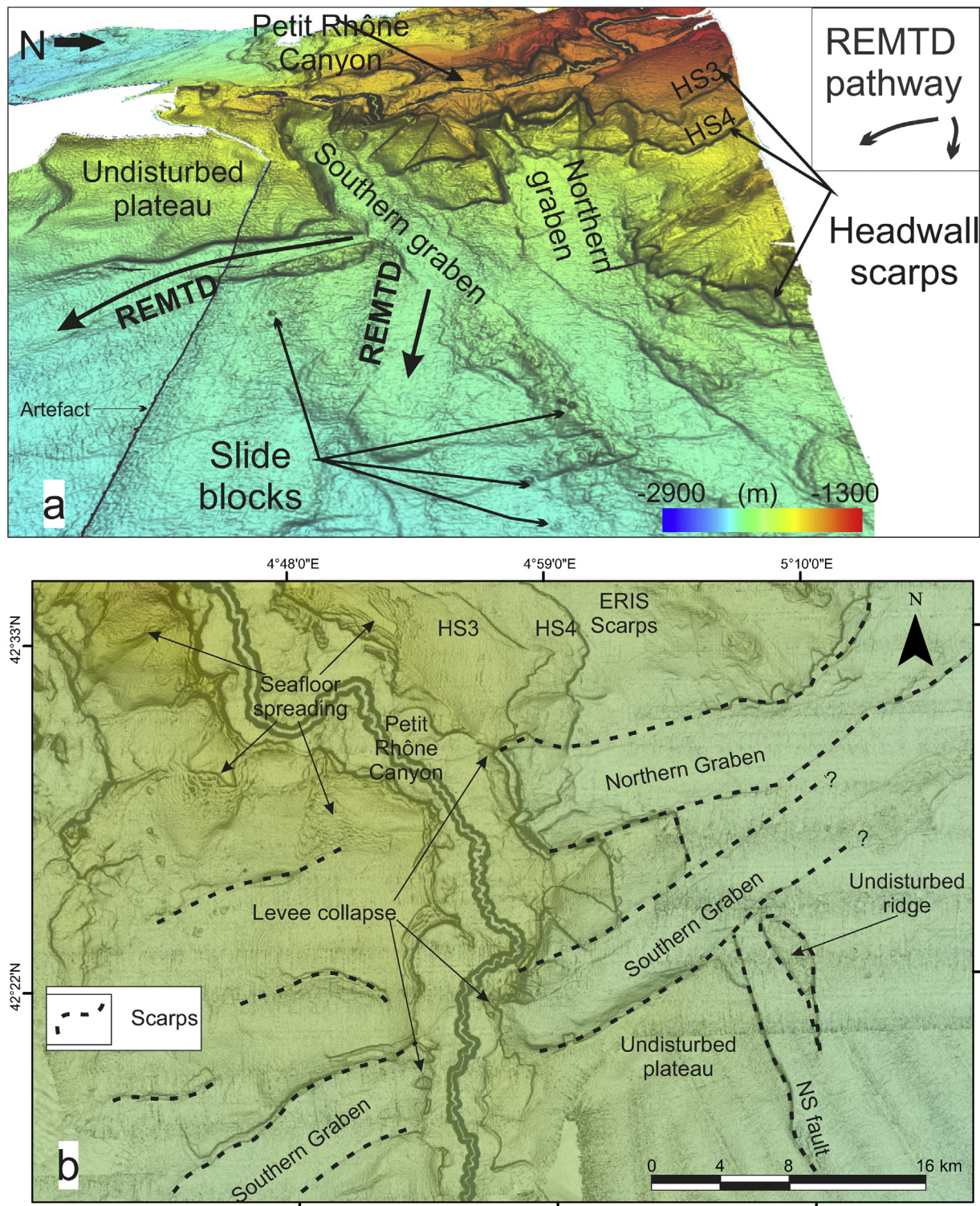


Fig. 3. a) Three-dimensional view of the toe area of the ERIS showing morphology of the fault grabens and a small slide lobe likely originating from the levee collapse. Vertical exaggeration 10 × . b) high-resolution bathymetric map of seabed morphology surrounding the toe area of the ERIS showing areas dominated by seafloor spreading, collapse of Petit Rhône Canyon levees and several scarps representing active faults as well as grabens.

MED-1 cruise (Rabineau et al., 2013). The processing sequence for the 2D HR MCS data includes quality control, filtering, binning, band-pass filtering, constant seawater velocity (1500 ms^{-1}) normal move out, stacking, and seawater velocity post-stack time migration. Seismic data from cruises PROGRES and AM-MED-1 were processed using Ifremer in-house softwares SISPEED and Solid-QC, respectively. Sub-bottom profiles (SBP) were collected during

several French oceanographic campaigns and checked for quality control with Ifremer software QC SUBOP (Table 1). A typical problem when imaging submarine landslides is the presence of diffraction hyperbolae generated at the edges of landslide scarps and steep slopes (see for example Fig. 4, in 2D HR MCS, and Fig. 4 Insets 1 and 2 in SBP) and/or within MTDs due to the presence of scattered blocks (Fig. 5b in 2D HR MCS; Fig. 5a Inset in SBP). Seis-

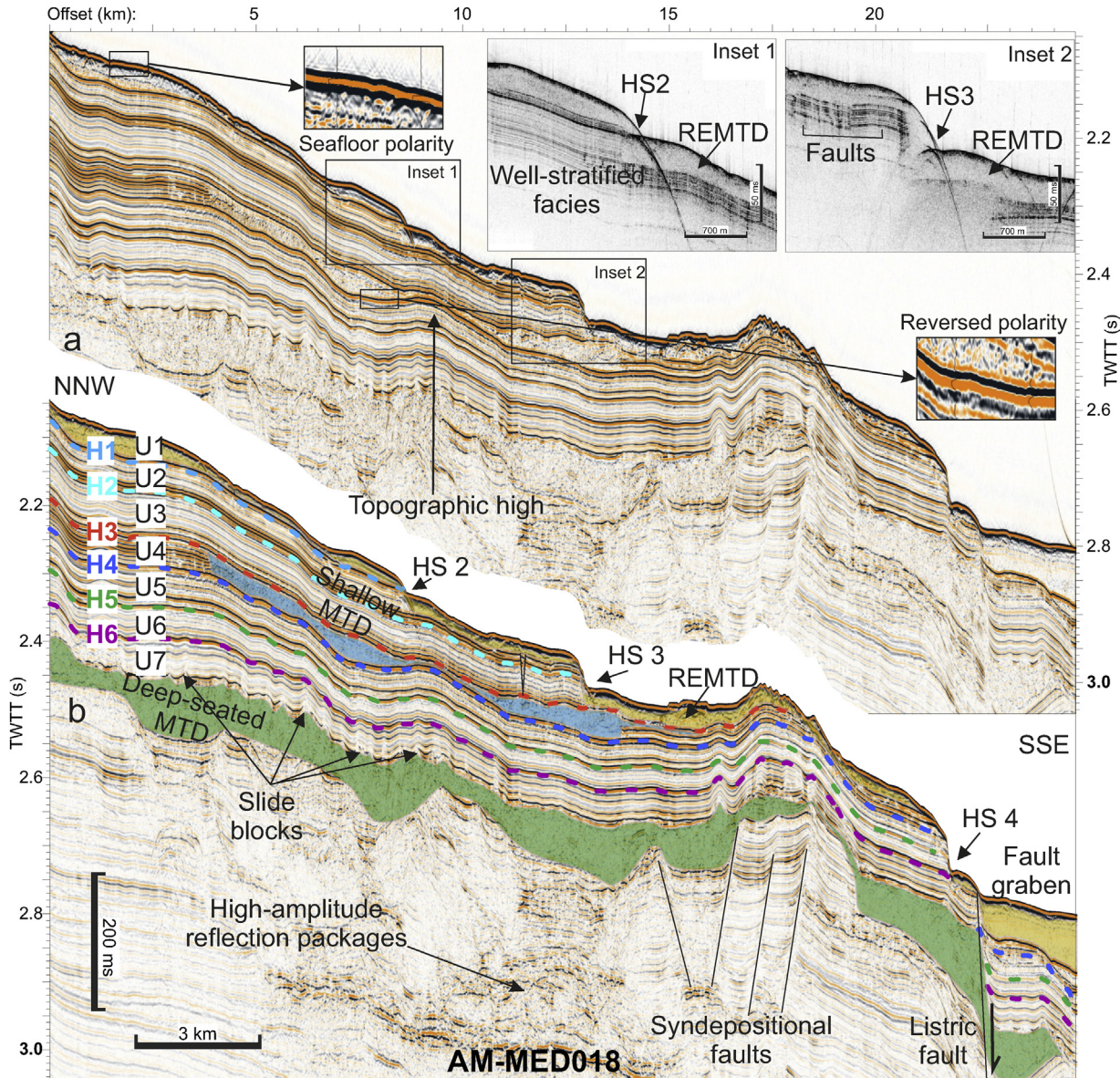


Fig. 4. a) Uninterpreted and b) interpreted dip seismic profile AM-MED018 (NNW-SSE) crossing the eastern part of the ERIS. It illustrates the sharp truncation of the headwall scarps, the surficial MTD (REMTD) and two buried MTDs - shallow MTD and deep-seated MTD (highlighted with blue and green colour, respectively). Insets 1 and 2 show blow-ups of headwall scars HS2 and HS3 in the sub-bottom profiles marked by sharp truncations of well-stratified sediments overlain by transparent reflections interpreted as MTD. Solid black lines represent prominent faults imaged in the seismic profile. The seismic stratigraphy of the study area is highlighted by seven key reflectors (H1 to H6) delineating 7 seismic units (U1 to U7). These key reflectors and seismic units are shown with the same respective colours and names in Figs. 5, 6, 7c and 8. Note the reversed polarity of horizon H4 with respect to the seafloor. See Fig. 2 for the location of the profile.

mic profiles collected during AM-MED-1 cruise show low frequency and low amplitude artefacts 40 ms below the seafloor, particularly in the areas of transparent reflections (Fig. 6). These artefacts are common in marine seismic acquisition and are associated to bubble pulse artefacts that are produced due to oscillations of the air bubble generated by an airgun. We have paid a special attention to these artefacts to avoid misinterpretation of seismic data.

For lithological characterization and age estimation of sedimentary facies, we used four sediment cores of 10–20 m long (PSM3-CS041, 42, 46 and 47), collected during cruise PRISME 3 (Cattaneo, 2013a) in the toe area of the ERIS using a Calypso Piston corer. Identification of lithofacies is based on visual description performed onboard. Geotek® Multi-Sensor Core Logger (MSCL) was used for gamma-density measurements at 1-cm interval. To obtain accurate ages of the slide events building up the REMTD, each core was carefully subsampled in the post-slide hemipelagic drape

to avoid contamination from reworked sediments, such as turbiditic deposits or bioturbation. Hence, these samples provide a minimum age for failure. Nine radiocarbon dates were determined by accelerator mass spectrometry (AMS). Dates were obtained from handpicked monospecific planktonic foraminifera (*Globigerina bulloides*) extracted from the hemipelagic sediments and were analyzed at the Beta Analytics, London, UK. Conventional ^{14}C years BP were converted into calibrated calendar ages with CALIB V7.1 (Stuiver et al., 2017) using the marine calibration curve Marine13 curve (Reimer et al., 2013) with a reservoir correction (ΔR) value of 48 ± 101 years and reported in this study with 2σ errors (Table 2). We used the same calibration procedure presented in (Dennielou et al., 2019) to allow for an easy comparison. All datasets were finally integrated and imported to the IHS Kingdom Software® for further joint interpretation.

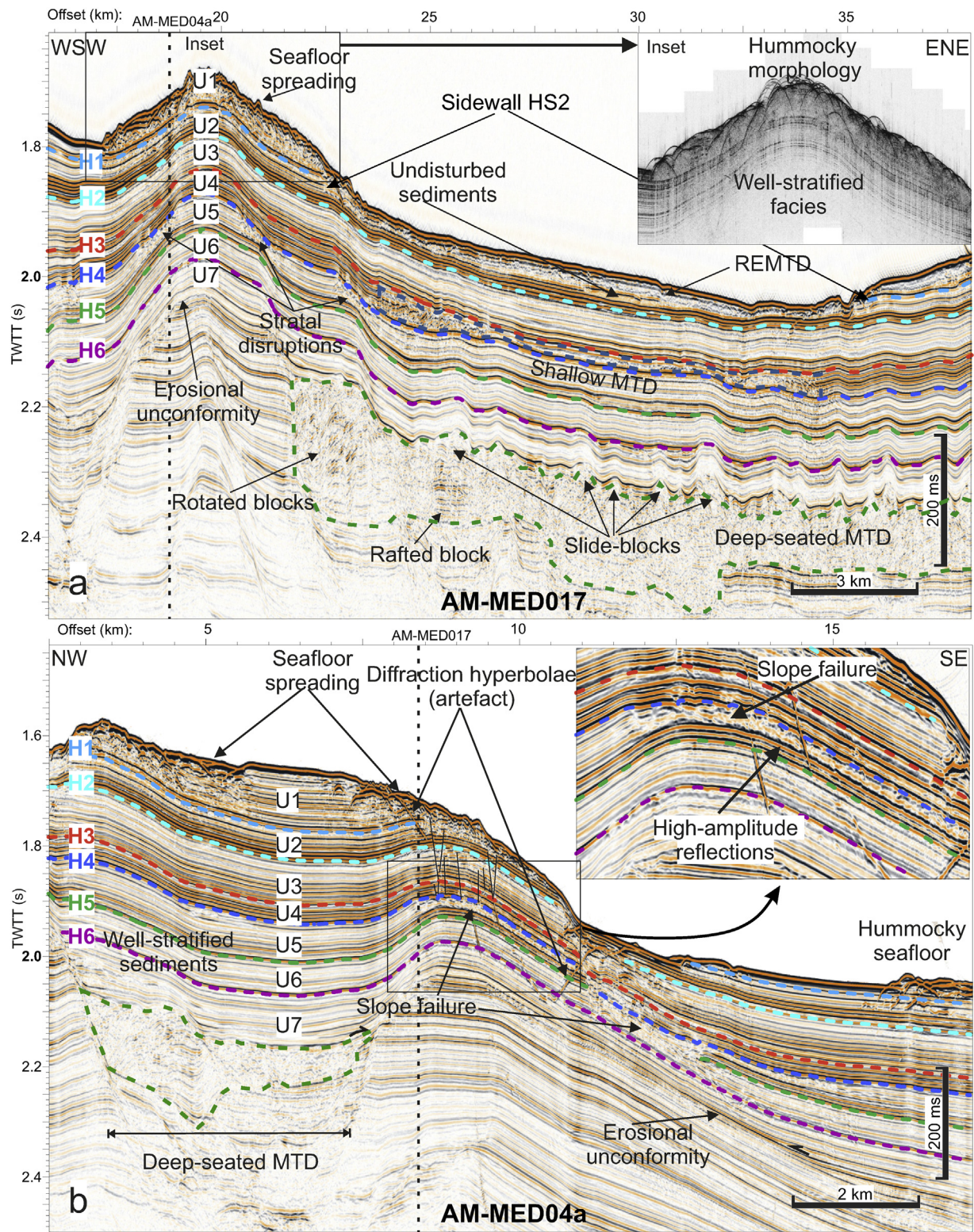


Fig. 5. a) Strike seismic profile AM-MED17 (oriented WSW-ENE) crossing the source area of the ERISC (in its proximal part). The profile images the sidewalls of headwall scar HS2 showing truncation of seismic unit U2, the Shallow Mass Transport Deposit (SMTD, blue rounded polygon, between H3 and H4) and the Deep-Seated Mass Transport Deposit (DSMTD, green rounded polygon, below 2.2 s twtt). The left part of the profile shows a transition of well-stratified sediments to chaotic reflections with intact internal reflections representing seafloor spreading above H1. The inset shows coinciding sub-bottom profile showing hummocky morphology with reflection hyperbolae, b) NW-SE oriented strike perpendicular seismic profile AM-MED04 shows a small-scale failure within seismic unit U5. See Fig. 2 for the location of the line.

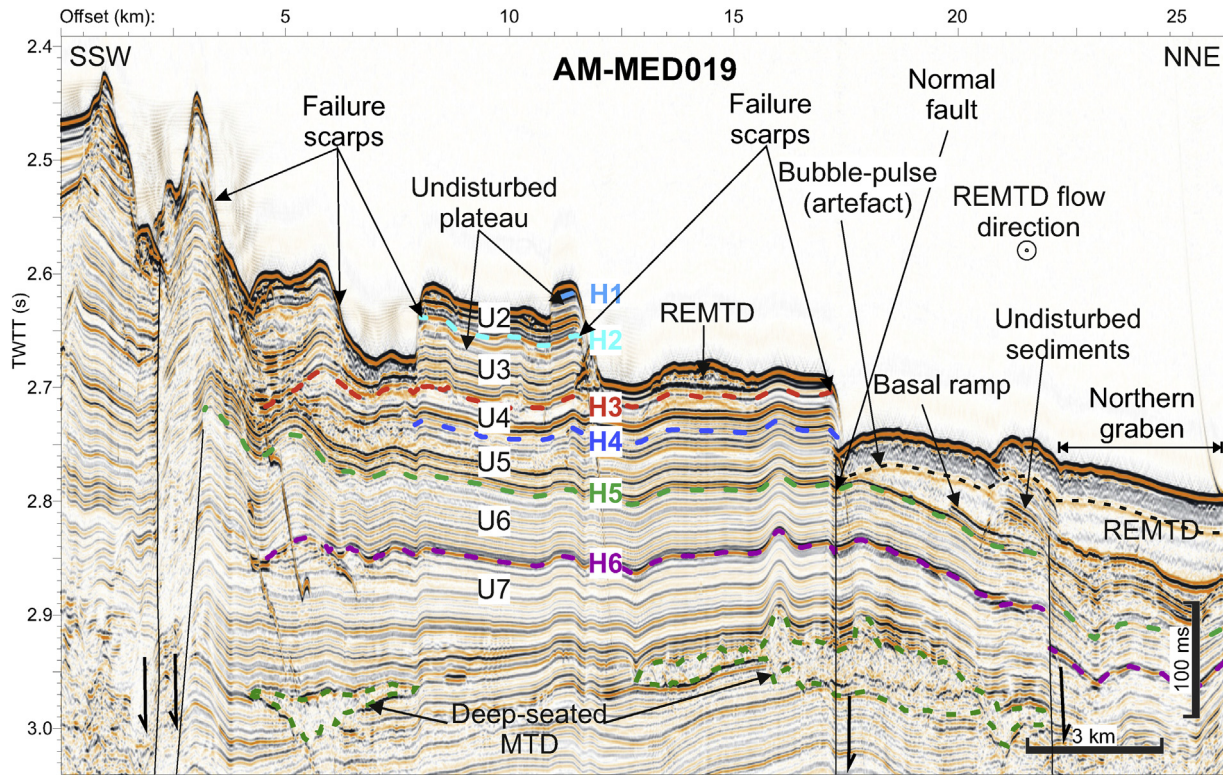


Fig. 6. SW-NE oriented, strike seismic profile AM-MED019 crossing the toe area of the ERISC about 25 km downslope of AM-MED17. The profile images sharp truncation of well-stratified seismic units at several levels indicative of failure surfaces. Note that the SMTD is not imaged in the profile suggesting a short run out of this landslide. The DSMTD is limited to two patches (marked by the dashed green line) of 50–100 ms thickness. The eastern and western parts of the profile are disturbed by normal faults. See Fig. 2 for the location of the profiles.

Table 2
Radiocarbon dating carried out on sediment cores.

Core-section-depth (m)	Lab reference	^{14}C age	Calibrated age (2σ) ^a	Sampled material
PSM3-CS042-S01-0.15	508495	13390 +/- 50 BP	15825 - 15140	<i>G. bulloides</i>
PSM3-CS042-S03-2.4	508496	16990 +/- 60 BP	20264 - 19612	<i>G. bulloides</i>
PSM3-CS042-S04-3.085	508497	17450 +/- 50 BP	20818 - 20171	<i>G. bulloides</i>
PSM3-CS042-S04-3.55	508498	18200 +/- 60 BP	21835 - 21103	<i>G. bulloides</i>
PSM3-CS046-S06-5.04	508499	16240 +/- 60 BP	19385 - 18,792	<i>G. bulloides</i>
PSM3-CS046-S07-6.94	510578	17770 +/- 60 BP	21262 - 20571	<i>G. bulloides</i>
PSM3-CS046-S08-6.965	508501	18150 +/- 60 BP	21785 - 21038	<i>G. bulloides</i>
PSM3-CS047-S07-6.10	510579	17120 +/- 50 BP	20446 - 19800	<i>G. bulloides</i>
PSM3-CS047-S08-7.6	508503	17380 +/- 50 BP	20710 - 20090	<i>G. bulloides</i>

^a Calibrated calendar ages were converted from conventional ^{14}C years BP with CALIB V7.1 (Stuiver et al., 2017) using the marine calibration curve Marine13 curve (Reimer et al., 2013) with a reservoir correction (ΔR) value of 48 ± 101 years and reported here as 2σ ages.

4. Results

4.1. Morphology

4.1.1. Overall morphology of the study area

The slope of the continental margin dips progressively from 6° to 1° for water depths leading from 200 m to 1500 m, respectively. Our study area, the interfluvial of the PRC and Grand Rhone Canyon (GRC), is characterised by a gentle slope of 1.8° and an area of about 1000 km^2 comparable to an open slope environment. The newly-acquired multi-beam bathymetric data show the seafloor morphology of the interfluvial area in greater detail than what has been published previously (Berné et al., 2002; Droz and Bellaïche, 1985; Torres et al., 1995). Our data show multiple distinct features related to mass-wasting processes such as slide scars, faulting activity, or seafloor spreading (Figs. 2 and 3b). The most prominent features in the study area are the NNW-SSE oriented lobate and trapezoidal-shaped scars in the bathymetry (black dashed lines in

Fig. 2) that we interpret as a suite of submarine landslides within the Eastern Rhone Interfluvial Slide Complex.

At a water depth of 1750 m, within the toe area of the ERIS, two SW-NE oriented linear depressions incise the seafloor (Figs. 2a, b and 3), previously interpreted as normal faults (dos Reis et al., 2005). However, we observe that these depressions are marked by significantly low-standing hanging block (~ 30 –40 m) bounded by normal faults that face opposite to each other (Figs. 2a and 3). Therefore, we interpret these depressions as fault grabens and refer to them hereafter as the Northern Graben (NG) and the Southern Graben (SG). The SG is about six km wide and extends over approximately 100 km in the SW-NE direction, crosscutting the entire Petit Rhone fan (Fig. 3). The NG shows a strike similar to that of SG, but it is limited to the west by the Eastern levee of the PRC. The northern scarp of SG displays a step-like morphology with a net slip of about 20–30 m, however, the southern wall shows gentler slopes of $\sim 5^\circ$ as compared to the 10 – 25° of that of the northern wall. The NG shows very steep scarps in the bathymetric data reaching up to

Table 3

Headwall height, length, area and volumes of the different failure steps of the Eastern Rhone Interfluve Slide (ERIS).

Headwall	Headwall height (m)	Evacuation length (km)	Average area (km ²)	Average volume (km ³)
HS1	60	38	650	39
HS2	30	25	380	15.2
HS3	50	20	350	31.3
HS4	70	16	140	9.8
SS	50	8	35	1.75
Eastern extension	150	10	165	9.75
Total				106.8

30° and creating almost an arcuate-shaped geometry comparable to a slope failure on the eastern levee (Figs. 2a, d and 3). Additionally, its location coincides with the foot of the ERIS. The NG shows a maximum net offset of 150 m where it coincides with the eastern levee of the PRC, however, the average offset of the faults is about 50 m and the average width is approximately seven km.

4.1.2. The Eastern Rhone Interfluve Slide (ERIS)

The ERIS consists of four main headwall scarps (named HS1 to HS4) and several secondary scarps (Fig. 2a-c). The average height of the headwall scarps ranges from 30 m to 70 m, but it exceeds 100 m in the area where the slide complex merges with the grabens, towards the eastern levee of the Petit Rhone Canyon. The headwalls are nested in a staircase style, with evidence of four major and several minor slide scarps with exposed glides planes (Fig. 2a, c). This geomorphological pattern is reminiscent of retrogressive failures such as reported in the Storegga landslide complex (Baeten et al., 2014; Bryn et al., 2005). The source area of the ERIS exceeds 700 km², covering almost 70 % area of the interfluve.

The headwall scarps of the slides have an irregular geometry, at times mimicking the shape of the previous scarps. The uppermost headwall of the slide (HS1) is located at a water depth of 700 m, only seven km away from the shelf-break. A minor failure scarp observed attached to the headwall scarp HS1 is interpreted as a secondary failure scarp of the HS1. The upper part of the HS1 is only 2.5 km wide, but it widens to about 25 km at 1700 m water depth. The average width of the slide is 20 km and the slide deposits (i.e. REMTD) are mapped as far as 200 km away from the source area (Droz and Bellaïche, 1985; Torres et al., 1997). Overall, a slope gradient of 1.8° characterises the Rhone interfluve; however, the slide scarps show a steep morphology with local slopes reaching up to 25–30°. The lowermost headwall scarp HS4 is located at 1700 m water depth, aligned perpendicularly with the NG. It extends 30 km towards the Grand Rhone sedimentary ridge, coinciding with the NG and showing a horseshoe-shaped landslide headwall morphology (Fig. 2a). The average area, height of headwall scarp, width of failure and volume of mobilized material of each slide scarp are summarized in Table 3. The total volume of mobilized material from the source area based on the geometry of each headwall scarp and of their respective height accounts to approximately 110 km³ (Table 3).

The deposit area of the ERIS (i.e. REMTD) is characterised by a smooth morphology. The sediment flow pathways of the mass-transport are mostly unnoticeable in the bathymetric data, most likely due to the post-slide sedimentary drape (Dennielou et al., 2019) and lack of high-resolution data in the deposit area (Figs. 1 and 2a). The overall flow direction of the REMTD is towards the southeast (Droz, 1983). In the newly-acquired high-resolution bathymetry, we observe few slide blocks of 10 m–25 m height and a bulge in the bathymetric data indicating minor pathway of the REMTD limited to the distal reach of the NG (Figs. 2a and 3 a). At a water depth of 2000 m, south of the SG, we observe a 250-km² plateau of undisturbed sediments, previously described as “butte témoin” by Droz (1983). This plateau is located between the PRC (towards the west) and a steep scarp of 80 m height (towards the east). About two km east of the plateau, we observe an N-S ori-

ented linear sediment ridge, which we interpret as the remnant of the failure. At the western ends of both grabens, we observe a breach of the eastern levee of the PRC (Fig. 3b), coinciding with the headwall scarp HS2, suggesting that a significant amount of canyon-sourced turbidites have most likely overflowed and been deposited together within the REMTD.

4.2. Sub-seafloor architecture

4.2.1. Seismic stratigraphy of the study area

Our study focuses on the mass-wasting processes within the upper part of Plio-Quaternary sediments. In this section, we describe the identified units and key reflectors that will let us discuss specific mass-wasting features we observe in a relative stratigraphic framework used in this study. For a detailed stratigraphic framework of the GoL, we refer to Droz et al. (2006) and Torres et al. (1995).

Seven seismic Units (U1 to U7, youngest to oldest, Figs. 4–7) are identified in the study area based on their reflection pattern and the erosional or depositional nature of contact with underlying sequences. The high-amplitude reflectors (H1–H7, top to bottom) at their bases define the boundaries of the units, which have been observed and picked extensively throughout the study area. Parallel, moderate to high-amplitude reflection packages in the whole study area characterise U1 to U7. The seismic units, in general, show a decreasing upward trend in internal reflection amplitudes. The contacts between seismic units are smooth and regular, except U7, which lies unconformably on the underlying sediments showing a rough morphology at its base. The average thickness of U2, U5, U6 and U7 is about 50 ms, while for U1, U3, and U4 it is about 100 ms.

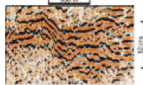
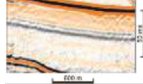
Four types of seismic facies are observed in the seismic sections (Table 4): 1) Moderate to high-amplitude well-stratified facies interpreted as turbiditic levee facies (Droz et al., 2006), 2) high-amplitude reflection packages (HARPs), similar to the ones observed in the Amazon Fan (Pirmez et al., 1997) interpreted here as coarse-grained material deposited within paleo-Rhone channel thalweg (Damuth, 1980; Droz et al., 2006), 3) Chaotic reflections interpreted as slide deposits (Droz et al., 2006) and 4) Acoustically transparent facies typical of REMTD and RWMTD (Dennielou et al., 2019; Droz et al., 2006)

4.2.2. Slides and failure planes

The dip seismic profile AM-MED18 shows the internal structure of the eastern side of the ERIS (Fig. 4). The source area is characterised by three distinct morphological steps of 30, 70 and 120 ms height, which correspond to the headwall scarps HS2, HS3 and HS4 respectively (Figs. 2a and 4). The scarps HS2 and HS3 truncate the seismic units U1 and U2 respectively, while scarp HS4 truncates units U6 to U1. Scarp HS4 coincides with the listric fault delineating the Northern Graben, which truncates the seismic units U3 and U4 (Fig. 4). The reflectors H2 and H3 mark the base units U2 and U3 that are truncated by the headwall scarps HS2 and HS3. The headwall scarps HS2 and HS3 cut through well-stratified sediments without crosscutting the underlying high-amplitude reflections, suggesting

Table 4

Summary of properties and interpretation of the seismic facies encountered in the study area.

Facies illustration	Reflection pattern	Continuity	Amplitude	Boundaries (upper/lower)	Depositional environment	Sedimentological interpretation
1		Parallel to sub-parallel	Continuous, semi-continuous, truncating	Moderate to low	Concordant	Upper-middle slope Hemipelagic nanofossil ooze, turbidites
2		Sub-parallel, irregular or hummocky	Variable, discontinuous	High	Discordant	Channel thalweg Coarse-grained channel deposits
3		Chaotic, hummocky	Discontinuous	Low to medium	Erosive (downlap/rough)	Upper-middle slope Slump deposits
4		Transparent	Discontinuous	Low	Concordant to erosive	Middle-lower slope Debris flow deposits

that the glide planes of the failures lie above the high-amplitude reflectors.

Interestingly, the glide planes of each failure have a similar dip as the seismic sequences, suggesting that the slides occurred parallel to the bedding surfaces and it is worth noting that the truncated facies mainly consist of low-amplitude reflections (Figs. 4 and 5a). This implies a strong stratigraphic control on the basal surfaces of the slide scars. Additionally, the basal reflectors display a reverse polarity with respect to the seafloor (Fig. 4). The amplitude of the reflections changes laterally at times but follows the normal trend of reversed polarity.

The strike profile AM-MED17 (Fig. 5a) crosses the sidewalls of the failure HS2. The sidewall of the failure is marked by the truncation of low-amplitude reflections over the high-amplitude basal surface H2. The profile clearly images 30-ms thick slide deposits characterised by chaotic to transparent acoustic facies typical for mass-transport deposits that we interpret as the results of uppermost failure (HS1) within the ERIS complex. These deposits distinctly contrast from the undisturbed, well-stratified turbiditic levee sediments.

Towards the western part of the ERIS, the uppermost failure appears like a transition of well-stratified sediments to chaotic reflections, with partly intact internal reflections above basal surface H1 (Fig. 5a, b). Of particular interest within the uppermost unit (U1) is the hummocky surface expressions, with downslope-dipping high-amplitude reflections showing "ridge and trough" morphology, which is particularly well identified showing reflection hyperbolae within the sub-bottom profiler data (Fig. 5a inset). Based on their seismic character and repetitive patterns of ridges and troughs oriented perpendicular to the direction of movement in the bathymetric data (Fig. 3b), we interpret these reflections as seafloor spreading similar to that observed within the Storegga slide complex (Micallef et al., 2007). Similar to the glide planes of failures originating from HS2 and HS3, the seafloor spreading observed in our data occurs locally above the high-amplitude reflector (H1 in this case).

Within the ERIS headwall area, we observe several erosional disruptions in the strata within the well-stratified facies, especially within unit U5, between reflectors H4 and H5 (Fig. 5a, b). These disruptions only affect unit U5, where a thinning of the entire unit of average thickness 100-ms to less than 50 ms is observed. In the areas of reduced thicknesses, we observe seismic facies related to slide deposits above the high-amplitude reflections. These disturbances occur locally in the areas of high relief approximately 200 ms

below the seafloor. We attribute these disturbances as a result of local slope failure related to an oversteepened slope that has been inherited from the morphology of the underlying sediments.

4.2.3. Internal seismic structure of the Rhone Eastern Mass-Transport Deposits (REMTD)

The REMTD appears as a body of transparent seismic reflections with low penetration in the sub-bottom profiler data (Figs. 6 and 7a, b). The REMTD seismic facies are homogeneous in most parts of the study area with very low to absent internal reflections or structures. It infills the seafloor depressions predating REMTD imaged in the study area (Fig. 7a). The average thickness of the REMTD is ~100 ms, with a maximum thickness of 150 ms in the depressions of the underlying strata. We observe several cases in the toe area of the ERIS, where the REMTD erodes the basal surfaces leaving behind the remnants in the form of basal ramps (Fig. 6).

At water depths between 2000–2200 m, along the western boundary of the REMTD, we recognize transformations in the structural style of the strata above reflector H4 (Fig. 7c). The proximal part of this area shows extensional features in the form of displaced and scattered blocks. The middle part consists of highly deformed and rotated blocks. The deformation becomes more apparent towards the front, with an increase in the degree of rotation. The frontal part of the area shows a compressional character with rather preserved stratigraphy in the form of pressure ridges with more than six individual blocks pushed upward from their original stratigraphy: we interpret these blocks as "pop-up blocks".

In the most distal area (in the deep basin), where the MTD pinches out to the seafloor, we observe ~5-ms high and 50-m long patches of transparent reflections in the sub-bottom profiles following the REMTD (Fig. 7b). As these patches appear individually over the basal surface of the MTD and are detached from the main MTD body, we interpret these patches as the "out-runner blocks", similar to that observed in the Nigerian continental slope (Nissen et al., 1999).

4.2.4. Buried MTDs

Within the Pleistocene sediments, we observe two buried MTDs that we refer to as "shallow MTD (SMTD)" and "deep-seated MTD (DSMTD)". The SMTD is observed within unit U4 between reflectors H3 and H4 (Figs. 4 and 5a). It displays well-stratified sediments at places but is mainly characterised by disturbed to chaotic seismic facies (Figs. 4 and 5a). As for ERIS, it is interesting to note that the glide plane of failure of the SMTD also occurs on top

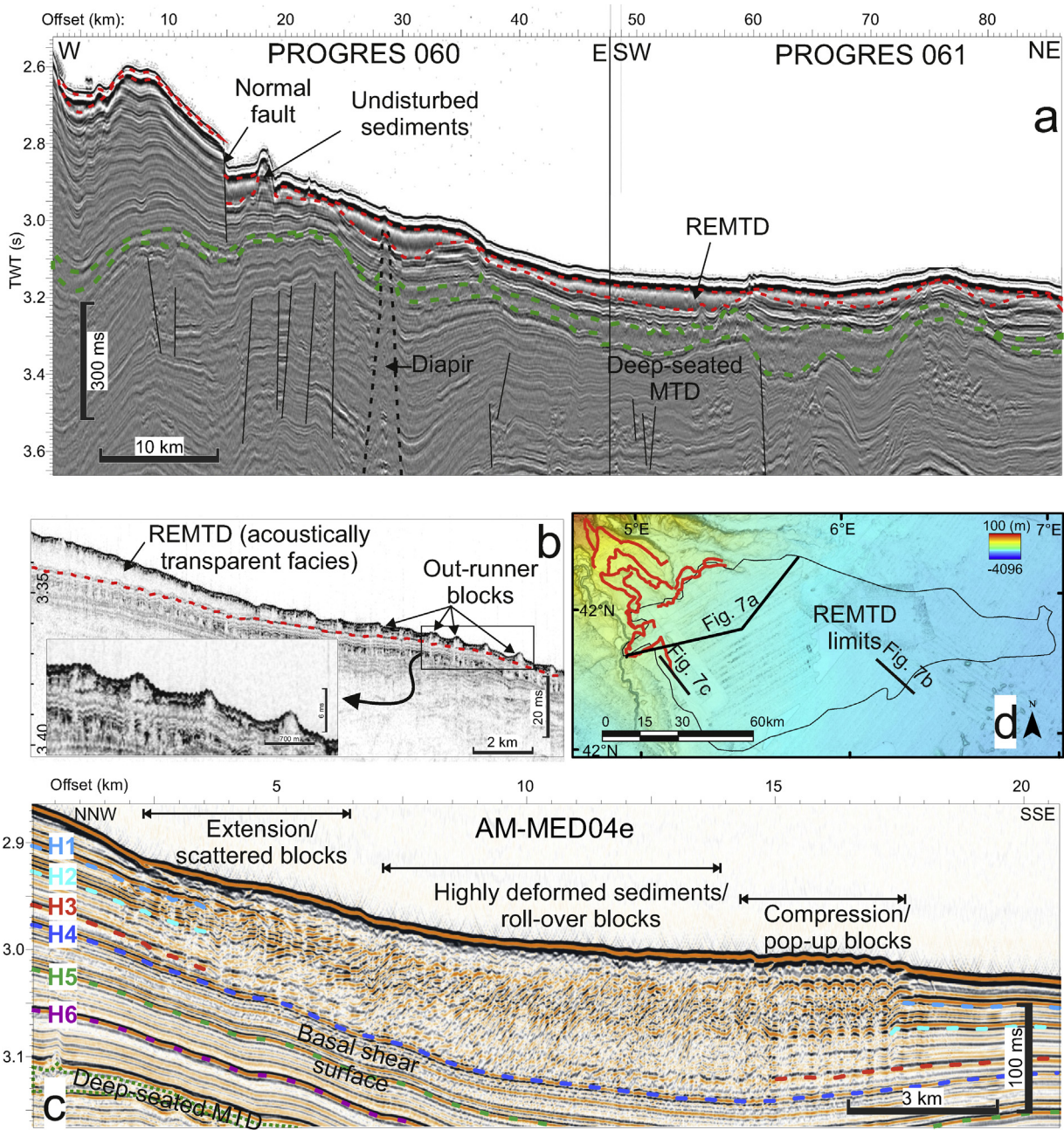


Fig. 7. a) Seismic profiles Progres 060 and 061 (SW-NE oriented) showing a transect through the REMTD. The colour scale of the seismic profile has been adapted for better visualization of the seismic data. b) NW-SE oriented sub-bottom profile crossing the southern limit of the REMTD showing patches of transparent facies interpreted as outrunner blocks. c) Extract of seismic profile AM-MED4e (NNW-SSE) through the compression ridge. d) Multibeam bathymetric map of the study area with profile locations.

of a high-amplitude horizon H4, without disturbing the underlying sediments (Figs. 4 and 5a). The average thickness of SMTD is approximately 40 ms; however, at the middle part of the SMTD, it crosses a local topographic high on which SMTD thins out to only five ms, healing the previous topography of the local high (Figs. 4 and 5a). The SMTD is observed locally, and the deposits are not found out of the interfluvium. This suggests an origin of the SMTD linked to a local slide with a very short run out distance, compared to that of the ERIS.

The DSMTD is observed 300 ms below the seafloor (Figs. 4–8) and is separated by about 150 ms thick sediments from SMTD. It covers a minimum area of about 3000 km², with an estimated minimum volume of about 400 km³ (Droz, 1983). The headwall scarp of DSMTD has not been mapped because of limitations in data coverage towards the north. However, based on its geom-

try, we infer a headwall location of DSMTD somewhere near the present-day shelf break, along the eastern levee of the PRC. DSMTD has a highly variable thickness ranging from 200 ms in the proximal area to 20–30 ms in the distal area. DSMTD deposits are mapped at least 100 km from the source area. The internal architecture of the DSMTD shows chaotic facies in the seismic data (Figs. 4 and 5a). In places, notably in the proximal area, the top boundary of the DSMTD is irregular showing ridge and troughs, appearing like mounds in the seismic profiles, which we interpret as coherent slide blocks and rafted blocks (Figs. 4 and 5). The basal surface of DSMTD is marked by a package of well-stratified sediments lying on the high-amplitude reflections of the paleo-canyon of the Petit Rhone fan (Torres et al., 1995). The contact of DSMTD with the underlying strata is uneven at places, eroding the underlying strata (Figs. 4 and 5a). The western part of the DSMTD is dominated by

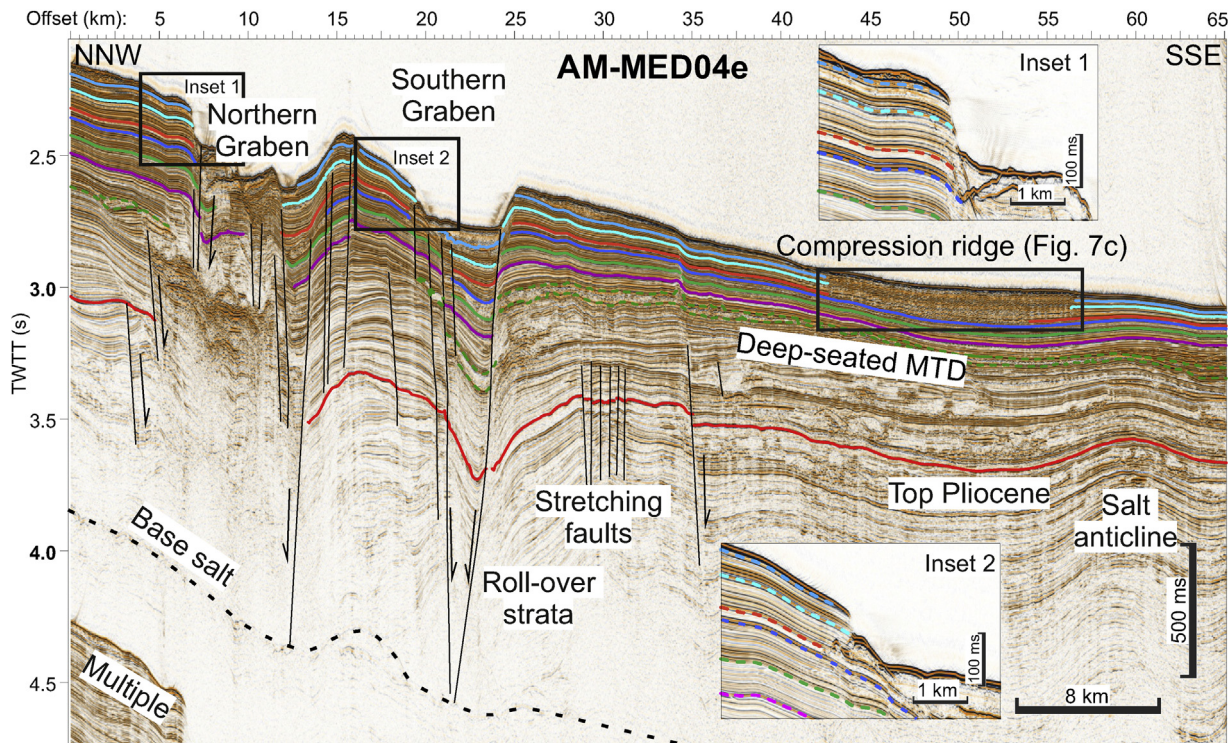


Fig. 8. Seismic profile AM-MED04e (NNW-SSE) crossing the study area showing NG and SG grabens formed by faults rooted to the base of the Messinian salt. Zoom of the fault scarps in inset 1 and 2 show recent scarps of height 100 ms and 40 ms respectively. See Fig. 2 for the location of the profile.

kilometre-scale rotated blocks identified by steeply dipping reflections (Fig. 5a). Next to the rotated blocks, we observe a 50-ms high and 1-km wide rafted block.

4.2.5. Faults

The entire GoL is dissected by several steeply dipping, low-amplitude anomalies interrupting the seismic reflections of the well-layered sediments and interpreted as normal faults. Faults in the GoL have been previously mapped and documented in detail using HR seismic and multibeam bathymetric data (dos Reis et al., 2015, 2005). dos Reis et al. (2015) reported the faults in the GoL as shelf-parallel, basinward-dipping and listric, rooted in the Messinian evaporite sequence. At least fifteen such faults have been documented in our study area, at times facing opposite to each other to form grabens that we named “Northern Graben (NG)” and “Southern Graben (SG)” (Fig. 8). These grabens have a dominant SW-NE trend and offsets in the range of 10–100 ms. In some cases, the faults have impacted the seafloor morphology and created bathymetric steps, therefore suggesting an active syn-Sedimentary salt tectonics until today. In addition to the SW-NE trending faults, we observe a local N-S trending fault along the undisturbed plateau offsetting the shallow strata down to 300 msbsf (Figs. 6 and 7a).

A close relationship seems to exist between the fault scarps and the failure planes of the ERIS. Especially at the toe of the ERIS, the scarp of the Northern Graben superimpose with the slide scar HS3 and HS4 where it forms a 50–100 ms high scarp (Figs. 4, 6, 8). To the west, the contact of the fault grabens with the Eastern levee of the Rhone canyon is characterised by truncations of the fan levees indicative of failure and collapse of the levee (Figs. 3a, b and 8). We observe that the scarps are only visible at the western and eastern-most parts of the ERIS, likely due to the alteration of the seafloor morphology after the deposition of the REMTD. Additionally, the eastward extent of the NG towards the GRC forms an elongated rupture in the bathymetry similar to that observed in slope fail-

ures. We thus interpret these scarps as the eastward extent of the ERIS complex (Figs. 2a and 3).

4.3. Lithology and age of sediment cores

Four sediment cores were recovered east of the Rhone submarine valley in the turbiditic levees; two in areas with a smooth bathymetry (PSM-CS041 & 42), two in areas with seafloor affected by mass-wasting (PSM-CS046 & 47). Lithological observations may be summarized into three lithofacies (L1 to L3; Fig. 9):

- Lithofacies L1 is composed of foraminifera and calcareous nannoplankton oozes that correspond to pelagic-hemipelagic sedimentation during the Holocene period (Fig. 9).
- Lithofacies L2 is composed of laminated clay with silt to very fine sand laminae interpreted as turbidites deposited by spillover from the Rhone valley (Dennielou et al., 2019).
- Lithofacies L3 is composed of stiff mud of generally higher bulk density than the background values ($1.85\text{--}1.90\text{ g.cm}^{-3}$). This lithofacies at times show colour banding corresponding to laminae and few silt layers characteristics of lithofacies in the Rhone fan (Dennielou et al., 2019; Lombo Tombo et al., 2015). The laminae are highly deformed and folded and show, at places, signatures of cracks. Based on the similarities observed in other studies in the study area (e.g. Bonnel et al., 2005; Dennielou et al., 2019, 2006; Lombo Tombo et al., 2015), we associate the lithofacies L3 to REMTD.

Core PSM3-CS41 was collected on the undisturbed plateau at 1996 m water depth and penetrated 19.33 m deep (Fig. 9). This core was acquired on the topographic high and samples only the background sediments, hence serves as a reference core for the study area. At the top, it presents 6 cm lithofacies L1. From 6 cm to the bottom of the core it presents lithofacies L2. The lithological uniformity of the core is well represented by the gamma density

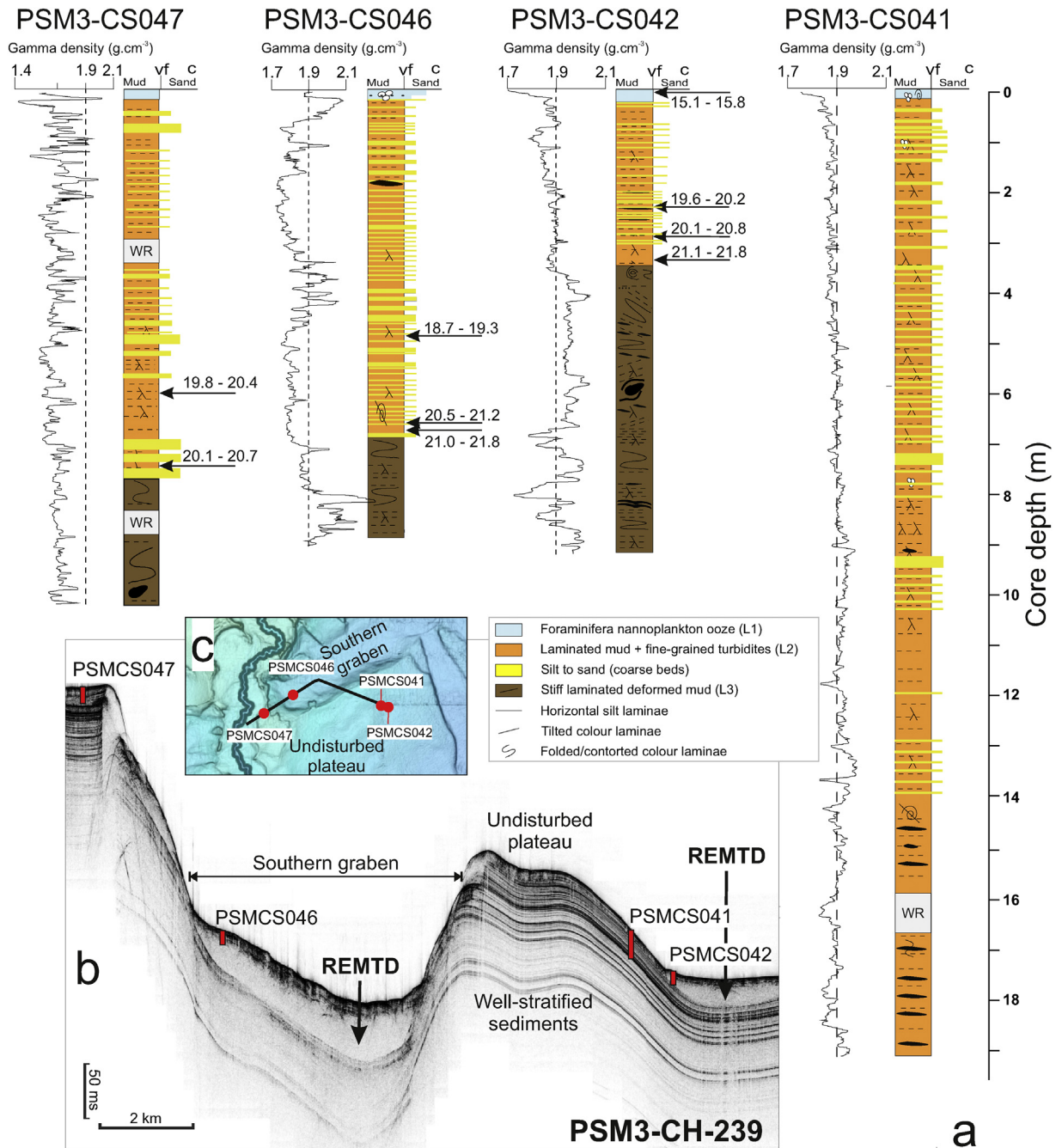


Fig. 9. a) Gamma density and lithofacies of sediment cores (from left to right, PSM3-CS047, 46, 42 and 41) collected at the toe of the Rhone Eastern Mass Transport Deposit (REMTD). b) Sub-bottom profile crossing the Southern Graben indicating the position and penetration of sediment cores (solid red rectangles). c) Location map of the sediment cores and the sub-bottom profile. WR: whole round samples collected for mechanical properties analysis (no lithostratigraphic description).

curve with bulk density falling between the background values 1.85–1.95 g.cm⁻³.

Core PSM3-CS42 is 9.29 m long and was collected at 2015 m water depth, one km east from core PSM3-CS41. The uppermost 20 cm of the core is composed of lithofacies L1. From 20 cm to 3.7 m, the core is composed of lithofacies L2. From 3.7 m to the bottom of the core it presents lithofacies L3. Sediments are highly deformed with steeply inclined and sometimes folded coloured bands. The inclination of the colour bands fluctuates through the core. The upper 3.7 m of the core is characterised by uniform bulk density lower than 1.9 g.cm⁻³, while below 3.7 m the bulk density values increase to 1.95–2.0 g.cm⁻³ and fluctuate throughout to the bottom of the core.

Core PSM3-CS46 was collected at 1985 m water depth and is 9.07 m long. The uppermost seven cm of the core is composed of lithofacies L1. From seven cm to 7.02 m, the core is composed of lithofacies L2 with silty laminae occurring every few cms. The frequency of the laminae decreases towards the top. From 7.02 m to the bottom of the core, below a sharp, erosive contact, the core presents lithofacies L3. The bulk density values for the top 7.02 m vary from 1.75 to 1.9 g.cm⁻³ and gradually increase to 2.05 g.cm⁻³ from 7.02 m towards the bottom of the core.

Core PSM3-CS47 is 10.87 m long and is located at the eastern flank of the PRC at a water depth of 1810 m. From the top to five cm, the core presents lithofacies L1. From five cm to 7.75 m, the core presents lithofacies L2. Similar to the core PSM3-CS46, this

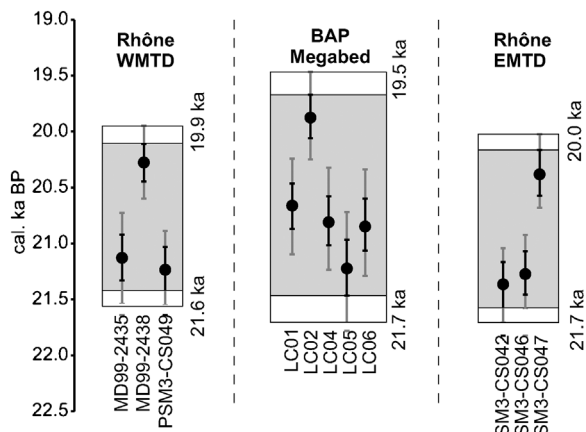


Fig. 10. Comparison of radiocarbon dates at the base of the post MTD drape on top of the REMTD (this study), RWMTD (Dennielou et al., 2019) and the Balearic Abyssal Plain Megabed (Rothwell et al., 1998).

part of the core shows frequent appearance of silty to sandy turbidites. However, the turbidites in this unit show erosive bases and are fining upwards. Below 7.75 m to the bottom of the core, the sediments show lithofacies L3. The bulk density values are well below the background values of $1.8\text{--}1.9\text{ g.cm}^{-3}$ throughout the core. The upper part of the core (down to 7.75 m) is characterised by density fluctuations whereas the lower part shows more stable values that generally increase towards the bottom of the core. However, the bulk density values for the entire core remain lower than the mean values observed in the other sediment cores.

Radiocarbon dating at the base of lithofacies L2, i.e. post-slide sediments within the undisturbed plateau, eastern PRC flank and the fault graben yield a 2σ age between 20 and 21.8 ka cal BP, with an average median age of 20.85 ka cal. BP (Fig. 9). The post-slide sediments dated in the cores at the base of the ERIS within the Southern Graben (core PSM3-CS46) and on the undisturbed plateau (core PSM3-CS42) yield a 2σ age between 21 and 21.8 ka cal BP, with an average median age of 21.4 ka cal BP. However, this does not discard the possibility of multiple stages of sliding within this time. We suggest that the younger ages at the eastern flank of the PRC (at the base of lithofacies L2 within the core PSM3-CS047, Fig. 9) relate to a younger failure ca 1 ka later than the main slide event. Our results coincide with the emplacement of RWMTD at 21 ka cal BP (Dennielou et al., 2019), suggesting a synchronous age for both MTDs (Fig. 10).

Our results are in general agreement with the previous studies that the sedimentation rates for the Holocene fall in the range of $0.05\text{ to }0.10\text{ m.ka}^{-1}$ whereas the sedimentation rates for the onset of the interglacial period, which concerns laminations of muddy to silty clay material that is interpreted as fine-grained turbidites, the sedimentation rates exceed 1 m.ka^{-1} .

5. Discussion

5.1. Emplacement, kinematics and timing of failures in the Eastern Rhône Interfluvial

Multiple headwall scarps HS1-HS4 in the ERIS complex suggest multiple failures in the source area. The presence of the REMTD facies within the uppermost headwalls in the seismic data (Figs. 4 and 5a) and the presence of several flat-lying glide planes suggest a retrogressive translational propagation of the failure, meaning that the failure started at the toe of the ERIS and propagated stepwise towards the shelf along the high-amplitude reflectors. Our results are consistent with previously published evi-

dence that the overall flow direction of REMTD was towards the southeast due to the inherited topography of the Rhône Fan (Droz et al., 2006); however, the better resolution of the newly-available data allows us to reconstruct more finely the slide flow based on small-scale morphological features resulting from the failure (Fig. 11).

The basal ramp observed at the toe of the ERIS (Fig. 6) is a crucial kinematic indicator of the flow direction of the REMTD. Our observation is in agreement with the general observation that the ramps trend perpendicular to the flow direction of the failed mass (Alves, 2015; Bull et al., 2009; Gawthorpe and Clemmey, 1985; Trincardi and Argani, 1990). We suggest that the presence of the N-S oriented fault next to the undisturbed plateau (Figs. 2a,a) have most likely funnelled and channelised the flow of the failed sediments, eventually enhancing the erosion of the seafloor. Alves et al. (2014) suggested that the presence of basal ramps is a key indicator relating to the combined effect of the erosional power of the MTD and seafloor morphology. Since the ERISC occurred in a gentle slope of 1.8° , we suggest that basal ramps at the toe of the ERIS show an erosional tendency of the mass movement. The minor topographic highs along the grabens (Fig. 3a,11) suggest the deposition of failed sediments originating from the levee collapse during the major slide event or at a later stage.

Similar to other large MTDs around the world (e.g. RWMTD, Dennielou et al., 2019; BIG'95 debris flow, Lastras et al., 2005; Sahara landslide, Li et al., 2017), the REMTD has a long runout distance of about 200 km and an average width of 50 km. It filled the topographic depressions forming a smooth seafloor and shows very little to no reflections in the seismic data along with its transparent facies in the sub-bottom profiler data (Figs. 1, 2a, 7 a, b). This evidence suggests that the emplacement of the REMTD was highly fluid and mobile, such as in the case of a debris flow (Lastras et al., 2005). These arguments in addition to the presence of transparent seismic facies within the REMTD are in agreement with the previous studies on submarine debris flow (e.g. BIG'95 debris flow, Lastras et al., 2005). Additionally, the large width of the REMTD suggests that it must have transformed downslope into a more fluidic flow that allowed it to spread laterally.

We observe a frontally confined pressure ridge at the western boundary of the REMTD (Fig. 7c). Pressure ridges are typical within the lobes of debris flows (Moscadelli and Wood, 2008) and provide information about the flow direction of the MTDs. However, considering that the pressure ridge occurred on a stratigraphic level much lower than the REMTD and it is not located in the direction of the main pathway of the REMTD, we discard a genetic link of the pressure ridge relating to the REMTD. Gamboa and Alves (2016) suggested that pressure ridges are common within minibasins surrounded by buried salt-related structures. Similarly, the pressure ridge in the study area occurs within a minibasin bounded by a buried diapir in the south and a buried roll-over anticline in the north (Fig. 8). Therefore, the emplacement of this pressure ridge was likely controlled by the growth of the underlying salt structures, by analogy to what suggested for the Brazilian Margin (Gamboa et al., 2011; Gamboa and Alves, 2016).

The recurrence of the MTDs (REMTD, SMTD, and DSMTD) at different stratigraphic intervals suggests a long history of mass-wasting in the Gol. The DSMTD has been previously described as the result of a westward shift of the paleo-Rhone valley during the Mid-Pleistocene that coincide with the occurrence of a major unconformity (~ 450 ka, Bellaiche et al., 1986; Droz, 1983; Droz et al., 2006; Torres et al., 1995). As for the SMTD, it has never been dated with direct or indirect methods. Based on the average sedimentation rates and its stratigraphic placement, we estimate that the SMTD was most likely emplaced around 350 ka. The REMTD, on the other hand has been directly dated, for the first time, using AMS radiocarbon dating. Radiocarbon dating of the post-REMTD

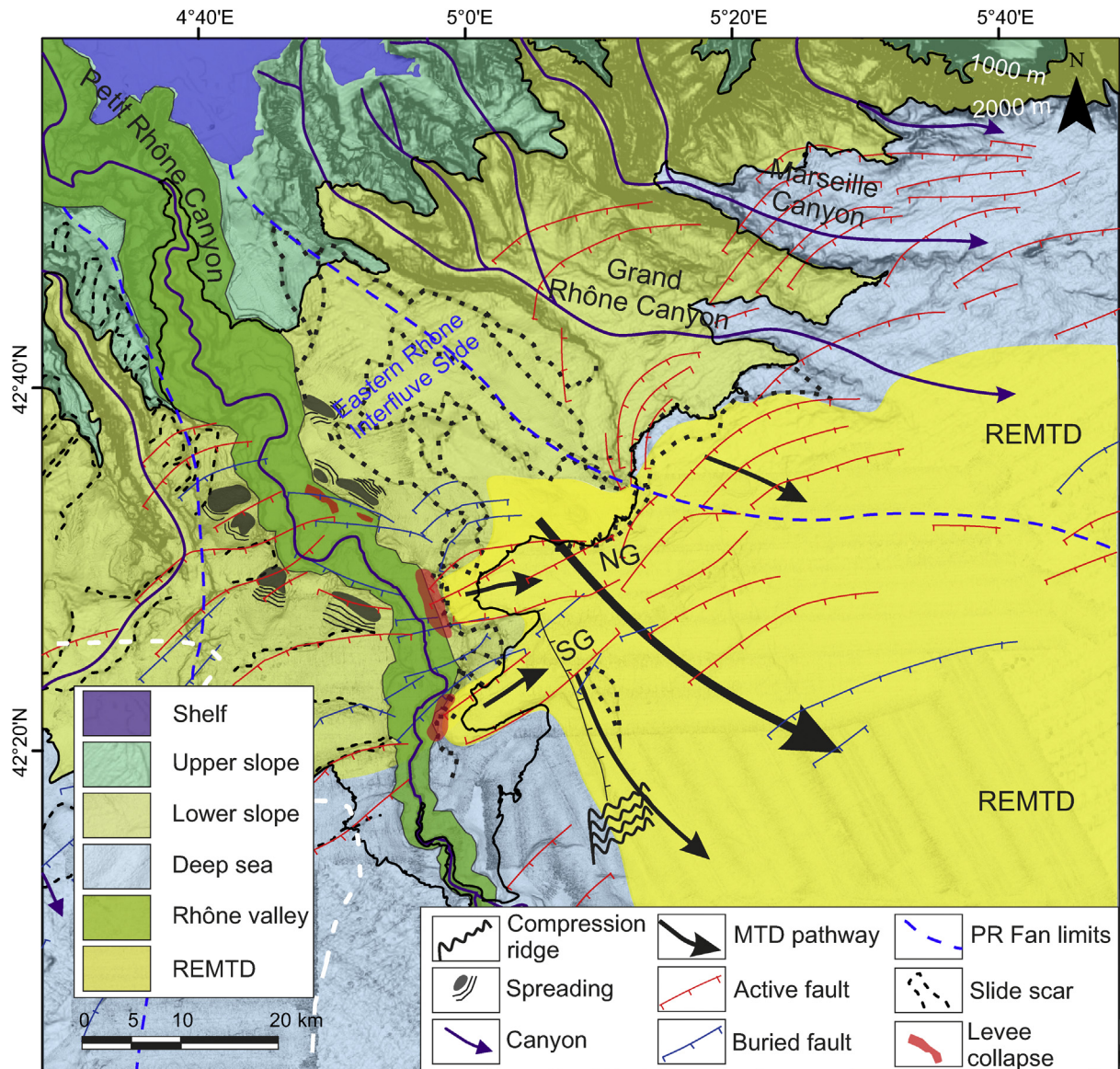


Fig. 11. Geomorphological interpretation map of the study area. REMTD: Rhône Eastern Mass Transport Deposit, NG: Northern Graben, SG: Southern Graben. Thick black arrows indicate probable main pathways of the REMTD. Active and buried faults are modified after dos Reis et al. (2005).

sediments confirms that it was emplaced between 21 and 21.8 ka cal BP (Figs. 9 and 10).

The ERISC took place before 21.4 ka cal BP, during the peak of the LGM, while the sea-level was 120 m lower than today. Within the resolution limits of geophysical data, we do not find evidence of multiple failure events. However, MTD lithofacies found on the Rhône levee (core PSM-CS047; Fig. 9) were deposited ca. 1 ka after the REMTD. This suggests that mass-wasting occurred over a long period of time, although not always in big volumes. Overall, the age of the emplacement of the REMTD from our study is coeval with the emplacement of the RWMTD (21.5 ka cal BP; Dennielou et al., 2019) and within dating uncertainties with the mega-turbidite in the Balearic Abyssal Plain (21.95 ka cal BP; Rothwell et al., 1998), suggesting a common trigger (Fig. 10).

5.2. The significance of the high-amplitude horizons in the ERIS

Glide planes of the ERIS, as well as the SMTD and pressure ridge, coincide with high-amplitude reversed polarity bedding planes

showing a strong stratigraphic control on the failures (Figs. 4–6, 7c). In the Western Mediterranean, repetition of these high-amplitude reflectors in the last six sedimentary sequences is attributed to 100 kyr-glacio-eustatic cycles in the upper slope successions in the GoL (Jouet et al., 2006; Rabineau et al., 2005; Sierro et al., 2009), in the Adriatic Sea (Ridente et al., 2009) and in the Tyrrhenian Sea (Toucanne et al., 2015). Especially in the GoL, the cyclicity expressed by the superposition of high-amplitude reflectors is widely reported as a result of deposition of condensed sections (Torres et al., 1995; Jouet et al., 2006; Rabineau et al., 2006, 2005; Riboulet et al., 2014; Sierro et al., 2009). Condensed sections are described as hard grounds representing long periods of geological time (Baraboshkin, 2009; Cattaneo and Steel, 2003; Crews et al., 2000; Loutit et al., 1988). In the GoL, these successions of condensed sections formed during periods of sea-level highstand, when sources of terrigenous sediments from the Alpine rivers shifted landwards. During highstands, deltaic sediments were trapped in the flooded inner shelf and hemipelagic sedimentation led to the preferential accumulation of pelagic skeletal

fractions in the lower slope (Frigola et al., 2012). We therefore suggest that the higher fractions of pelagic skeletal material as observed in the condensed sections in the PROMESS borehole (Jouet, 2007; Riboulot et al., 2014; Sierro et al., 2009), most likely create high bulk porosities in the sediments and eventually explain the reversed polarities identified in our seismic data (Figs. 4–6, 7c).

Submarine landslides can take place at slopes as gentle as 1° along potential weak layers, when the shear stress becomes significantly higher than the shear strength (Fields et al., 1982; Urlaub et al., 2015, 2018). Weak layers consist of sediments that have strengths lower than the adjacent layers to provide a potential focus for the development of the surface of rupture (*sensu* Locat et al., 2014). In high-latitude settings, as in the case of the Storegga slide complex, lithological contrast has been invoked as the main reason for developing weak layers, where contouritic and hemipelagic sediments are interbedded with glacigenic debris flow deposits (Laberg and Camerlenghi, 2008). Also in mid-latitude deepwater environments such contrast in lithology exists. Dan et al. (2009) invoked that lithological contrast of marine mud and thin-bedded turbidites could become an important predisposing factor in order to emplace major failures on the slopes. Condensed sections are composed of clayey sediments that are abundant of microfossils and could represent a significant contrast in lithology. They show higher shear strength than the overlying sequences and are well accepted as glide plane of the failure rather than to have acted as a weak layer, as proposed in the Ursa Basin (Sawyer et al., 2009; Sawyer and Hodelka, 2016) and in the Adriatic Sea (Sultan et al., 2008). The turbiditic sequences sandwiched between the condensed sections within the ERIS complex most likely control the localisation of potential weak layers, especially because coarser-grained materials (such as turbidites) are prone to liquefaction even in case of a mild seismic loading (Dan et al., 2009). This could explain why a variety of mass movements occur extensively over the high-amplitude horizons at several stratigraphic levels in the study area (Figs. 4–6, 7c).

5.3. Preconditioning and trigger mechanisms

The potential relationship between sea-level and landslide frequency has long been in the debate (Lee, 2007.; Leynaud et al., 2009; Owen et al., 2007; Urlaub et al., 2013). Urgeles and Camerlenghi (2013) highlighted an increase in landslide activity in the Mediterranean region during and after the LGM. Besides, Brothers et al. (2013) proposed a direct link between sea-level induced seismicity and slope failures. Even if some uncertainties remain on dating accuracies (Urlaub et al., 2013), and with limited analysis, it is difficult to directly demonstrate a causal link between climatic forcing and seafloor instabilities. Considering the synchronicity in the ages of multiple MTDs, we suggest that it should not be discarded that the sea-level fall during the LGM directly or indirectly played a major role in the emplacement of these large MTDs in the Western Mediterranean. Therefore, we discuss the likelihood of large-scale triggers that may have induced slope instabilities and eventually favoured emplacement of these large MTDs (especially REMTD and RWMTD) in the GoL.

Rapid sedimentation and excess pore-pressure generation: Rapid sedimentation can govern the stress and strength conditions on a slope over time, leading to failure, once a critical amount of preconditioning is reached (Stoecklin et al., 2017). The Rhone fan during the end of the last glacial period received sediment load up to 5 times the present-day during early phases of glaciers melting (Kettner and Syvitski, 2009; Lombo Tombo et al., 2015; Sierro et al., 2009). For instance, up to 25 m of sediments were deposited within 12 ka between 30–18 ka on the upper slope (Sierro et al., 2009) and four m of sediment were deposited in the Rhone turbiditic valley within 1.4 ka at the end of the LGM (Lombo Tombo et al., 2015).

Additionally, below-average bulk density (<1.9 g.cm⁻³) may suggest an under-consolidated state of the turbiditic units (Lithofacies L2; Fig. 9) that were deposited until the onset of interglacial period. Slope failure analysis at the Bourcart Canyon head show that sediment loading with only two m of sediment rapidly accumulated can generate significant slope failure (Sultan et al., 2007). Even if the morphology and sedimentary processes on the fan levees and at the base of the slope are different from those of canyon heads. One can assume that the much thicker accumulation on the open slope and fan levees must have favoured the failure. This forcing is further suggested by the age of the REMTD, between 20–21.7 ka cal BP (Fig. 10), exactly during the maximum lowstand and before the onset of sea-level rise (Clark et al., 2004; Lambeck et al., 2014), when rivers and canyons were connected to the shelf edge, maximum sediment loading occurred on the upper slope and maximum sediment was transferred to the rise and onto basin fans. The threshold between shear strength and stress under high accumulation rates could likely be reached, particularly because it can generate excess pore pressure and develop weak layers (Leynaud et al., 2007; Locat et al., 2014). In our case sedimentation rates, in the order of 1–2 m.ky⁻¹ (Lombo Tombo et al., 2015; Sierro et al., 2009) are not extreme like on glaciated margins (Hjelstuen et al., 2004), prodeltas (Fanget et al., 2013; Zhou et al., 2016) or even on deep-sea turbiditic channel mouth lobes (Dennielou et al., 2017; Rabouille et al., 2017). However, sub-seafloor architecture at places (especially within the ERIS headwall area) reveals steep slopes inheriting topographies of previous failures accompanied by local slope failures (e.g. Figs. 5a, b). The concurrence of over-steepening and low shear strength and under-consolidation by high sediment accumulation could constitute an aggravating factor for sliding. In addition to sediment loading and over-steepening, the occurrence of potential weak layers like silt layers may be determinant in the trigger of sliding (Dan et al., 2009; Locat et al., 2014). Therefore the porous silt layers occurring in the leveed turbiditic facies (Fig. 9) may have promoted an increase in excess pore pressure and have favoured sliding, particularly because they are sandwiched between clay-rich, less permeable layers.

Gravitational gliding of post-Messinian strata related to halokinesis: In the Gulf of Lions listric faults related to salt-sediment interactions extend from the base of the Plio-Quaternary (ca. two km deep). The majority of the faults reach the seafloor corresponding to escarpments with vertical offsets exceeding 20 m (dos Reis et al., 2005), suggesting an ongoing slope steepening due to salt-sediment interaction. Growth strata at the footwall of the NG and SG clearly show that the faults were most likely active at the time of emplacement of ERIS (Figs. 4,6,8). Therefore, an aseismic slip of the main growth fault may likely have resulted in a regional steepening of the seafloor and most importantly exposing the strata at the toe of the ERIS. In either case, the growth fault controls the location of the headwall scarps and with a slip of about 100 m an external trigger might not have been required, a high-sedimentation rate coupled with high slope angles might have been enough to initiate the failure (Stoecklin et al., 2017).

Considering the coinciding ages of RWMTD (Dennielou et al., 2019) and REMTD (this study) at the peak of the LGM, and the presence of the faults crosscutting the entire GoL, we suggest that the growth faults located at the toe of the ERIS in presence of preferential failure planes and high-sedimentation rates most likely favoured the emplacement of the slide. Vertical movements of listric faults due to isostatic rebound may likely occur preferentially during the lowstand and be a positive feedback of sediment loading on the Rhone fan. Although the rate of vertical movements is not quantified, we suggest that it can be definitely considered as a further factor for sediment instability that adds up to high sediment accumulation.

6. Conclusions

The Gulf of Lions is a passive margin of about 200 km length and 70 km width with main sediment supply from the Rhone River depositing alpine sediments on the Rhone delta. The slope of the GoL is dissected by fifteen submarine canyons, the largest one being the Petit Rhone Canyon. Seafloor instability in the GoL occurs in canyon heads and flanks, but also in the interfluvial slope areas and the levees of the main submarine valleys. Previous studies highlighted the presence of several large surficial MTDs with volumes exceeding 100 km³. We presented here details on the REMTD that was emplaced 21.4 ka during the peak of the Last Glacial Maximum. The newly available high-resolution geophysical data allowed a detailed investigation of the source of the REMTD that we referred to as the Eastern Rhone Interfluvial Slide. The combination of a diversified geophysical dataset provides insights into the slope failure processes that can be summarised in the following points.

- The overall morphology of the ERIS is dominated by staircase geometry indicative of a retrogressive failure on multiple glide planes, extending from a water depth of 500 m–2000 m.
- Preconditioning of the ERIS by localization of weak layers may have been favoured by rapidly accumulated turbiditic sequences sandwiched between reversed polarity strong reflectors interpreted as condensed sections, which were most likely deposited during the sea-level highstands.
- The location of landslide scars seems to be associated with the presence of listric faults rooted in the Messinian evaporite layer acting as a décollement surface, driven by the gravitational gliding of post-Messinian strata.
- The triggering mechanism responsible for the emplacement of the slide is not yet clear, but a combination of processes such as local and regional slope steepening due to halokinesis and excess pore pressure generation due to rapid sediment accumulation likely affect the slope stability.

Data availability

Sediment cores are curated at IFREMER core repository in Plouzané (France). Core data related to this article can be requested at:

- Core PSM3-CS041: IGSN BFBGX-87805 (<http://igsn.org/BFBGX-87805>)
- Core PSM3-CS042: IGSN BFBGX-87806 (<http://igsn.org/BFBGX-87806>)
- Core PSM3-CS046: IGSN BFBGX-87810 (<http://igsn.org/BFBGX-87810>)
- Core PSM3-CS047: IGSN BFBGX-87811 (<http://igsn.org/BFBGX-87811>)

Acknowledgement

We thank the captains, crew and science parties of the PRISME-2 and PRISME-3 campaigns onboard R/V L'Atalante and R/V Pourquoi pas?, respectively for their support during the campaigns. The PhD of Shray Badhani is funded by the European Union's Horizon 2020 research and innovation programme under the Marie-Skłodowska-Curie grant via project ITN-SLATE (grant agreement No 721403). Sylvain Bermel, Mathilde Pitel Roudot and Arnaud Gaillot are thanked for their help on GIS data processing. This study has been greatly benefitted from several fruitful discussions with Shane Murphy, Jacques Déverchère and Elodie Lebas. We also thank Tiago M. Alves and an anonymous reviewer for their comments that significantly improved our manuscript.

References

- Alves, T.M., 2015. Submarine slide blocks and associated soft-sediment deformation in deep-water basins: a review. *Mar. Pet. Geol.* 67, 262–285, <http://dx.doi.org/10.1016/j.marpetgeo.2015.05.010>.
- Alves, T.M., Strasser, M., Moore, G.F., 2014. Erosional features as indicators of thrust fault activity (Nankai Trough, Japan). *Mar. Geol.* 356, 5–18, <http://dx.doi.org/10.1016/j.margeo.2013.07.011>.
- Baeten, N.J., Laberg, J.S., Vanneste, M., Forsberg, C.F., Kvalstad, T.J., Forwick, M., Vorren, T.O., Hafslidason, H., 2014. Origin of shallow submarine mass movements and their glide planes—Sedimentological and geotechnical analyses from the continental slope off northern Norway. *J. Geophys. Res. Earth Surf.* 119, 2335–2360, <http://dx.doi.org/10.1002/2013F003068>.
- Baraboshkin, E.Y., 2009. Condensed sections: terminology, types, and accumulation conditions. *Moscow Univ. Geol. Bull.* 64, 153–160, <http://dx.doi.org/10.3103/S0145875209030028>.
- Bassetti, M.A., Berné, S., Jouet, G., Taviani, M., Dennielou, B., Flores, J.-A., Gaillot, A., Gelfort, R., Lafuerza, S., Sultan, N., 2008. The 100-ka and rapid sea level changes recorded by prograding shelf sand bodies in the Gulf of Lions (Western Mediterranean Sea). *Geochem. Geophys. Geosyst.* 9, <http://dx.doi.org/10.1029/2007GC001854>, n/a-n/a.
- Bassetti, M.A., Jouet, G., Dufois, F., Berné, S., Rabineau, M., Taviani, M., 2006. Sand bodies at the shelf edge in the Gulf of Lions (Western Mediterranean): deglacial history and modern processes. *Mar. Geol.* 234, 93–109, <http://dx.doi.org/10.1016/j.margeo.2006.09.010>.
- Bellaïche, G., Coutellier, V., Droz, L., 1986. Seismic evidence of widespread mass transport deposits in the Rhône deep-sea fan: their role in the fan construction. *Mar. Geol.* 71, 327–340, [http://dx.doi.org/10.1016/0025-3227\(86\)90076-9](http://dx.doi.org/10.1016/0025-3227(86)90076-9).
- Berné, S., 2000. MARION cruise, RV Le Suroît, <http://dx.doi.org/10.17600/20110>.
- Berné, S., Dennielou, B., 2008. RHOSOS cruise, RV Le Suroît, <http://dx.doi.org/10.17600/8020040>.
- Berné, S., Gorini, C., 2005. The Gulf of Lions: an overview of recent studies within the French 'Margins' programme. *Mar. Pet. Geol.* 22, 691–694, <http://dx.doi.org/10.1016/j.marpetgeo.2005.04.004>.
- Berné, S., Jouet, G., Bassetti, M.A., Dennielou, B., Taviani, M., 2007. Late Glacial to Pre-boreal sea-level rise recorded by the Rhône deltaic system (NW Mediterranean). *Mar. Geol.* 245, 65–88, <http://dx.doi.org/10.1016/j.margeo.2007.07.006>.
- Berné, S., Satra, C., Aloïsi, J.C., Baztan, J., Dennielou, B., Droz, L., Dos Reis, A.T., Lofi, J., Méar, Y., Rabineau, M., 2002. *Carte morpho-bathymétrique du Golfe du Lion, notice explicative*. Ifremer, Brest 48.
- Bonnel, C., Dennielou, B., Droz, L., Mulder, T., 2005. Architecture and depositional pattern of the Rhône Neofan and recent gravity activity in the Gulf of Lions (Western Mediterranean). *Mar. Pet. Geol.* 22, 827–843, <http://dx.doi.org/10.1016/j.marpetgeo.2005.03.003>.
- Brothers, D.S., Luttrell, K.M., Chaytor, J.D., 2013. Sea-level-induced seismicity and submarine landslide occurrence. *Geology* 41, 979–982, <http://dx.doi.org/10.1130/G34410.1>.
- Bryn, P., Berg, K., Stoker, M.S., Hafslidason, H., Solheim, A., 2005. Contourites and their relevance for mass wasting along the Mid-Norwegian Margin. *Mar. Pet. Geol.* 22, 85–96, <http://dx.doi.org/10.1016/j.marpetgeo.2004.10.012>.
- Bryn, P., Solheim, A., Berg, K., Lien, R., Forsberg, C.F., Hafslidason, H., Ottesen, D., Rise, L., 2003. The Storegga Slide Complex; Repeated Large Scale Sliding in Response to Climatic Cyclicity. Springer, Dordrecht, pp. 215–222, <http://dx.doi.org/10.1007/978-94-010-0993-2-2.24>.
- Bull, S., Cartwright, J., Huuse, M., 2009. A review of kinematic indicators from mass-transport complexes using 3D seismic data. *Mar. Pet. Geol.* 26, 1132–1151, <http://dx.doi.org/10.1016/j.marpetgeo.2008.09.011>.
- Cara, M., Cansi, Y., Schlupp, A., Arroucau, P., Béthoux, N., Delouis, B., Denieul, M., Deschamps, A., Doubre, C., Fréchet, J., 2015. SI-Hex : a new catalogue of instrumental seismicity for metropolitan France. *Bull. La Soc. Geol. Fr.* 186, 3–19, <http://dx.doi.org/10.2113/gssgbull.186.1.3>.
- Carvajal, M., Araya-Cornejo, C., Sepúlveda, I., Melnick, D., Haase, J.S., 2019. Nearly instantaneous tsunamis following the mw 7.5 2018 palu earthquake. *Geophys. Res. Lett.* 2019, GL082578, <http://dx.doi.org/10.1029/2019GL082578>.
- Cattaneo, A., 2013a. PRISME 3 cruise, RV Pourquoi pas?, <http://dx.doi.org/10.17600/13030060>.
- Cattaneo, A., 2013b. PRISME 2 cruise, RV L'Atalante., <http://dx.doi.org/10.17600/13010050>.
- Cattaneo, A., Steel, R.J., 2003. Transgressive deposits: a review of their variability. *Earth-Science Rev.* 62, 187–228, [http://dx.doi.org/10.1016/S0012-8252\(02\)00134-4](http://dx.doi.org/10.1016/S0012-8252(02)00134-4).
- Clare, M., Chaytor, J., Dabson, O., Gamboa, D., Georgiopoulou, A., Eady, H., Hunt, J., Jackson, C., Katz, O., Krastel, S., León, R., Micallef, A., Moernaut, J., Moriconi, R., Moscardelli, L., Mueller, C., Normandea, A., Patacci, M., Steventon, M., Urlaub, M., Völker, D., Wood, L., Jobe, Z., Geology, M., Surveying, S., 2018. A consistent global approach for the morphometric characterization of subaqueous landslides, <http://dx.doi.org/10.1144/SP477.15>.
- Clark, P.U., McCabe, A.M., Mix, A.C., Weaver, A.J., 2004. Rapid rise of sea level 19,000 years ago and its global implications. *Science (80-)* 304, 1141–1144.
- Cochonat, P., 2001. GMO1 cruise, RV Le Suroît, <http://dx.doi.org/10.17600/1020040>.
- Crews, J.R., Weimer, P., Pulham, A.J., Waterman, A.S., 2000. Integrated approach to condensed section identification in intraslope basins, Pliocene-Pleistocene, northern Gulf of Mexico. *Am. Assoc. Pet. Geol. Bull.* 84, 1519–1536.
- Damuth, J.E., 1980. Use of high-frequency (3.5–12 kHz) echograms in the study of near-bottom sedimentation processes in the deep-sea: a review. *Mar. Geol.* 38, 51–75, [http://dx.doi.org/10.1016/0025-3227\(80\)90051-1](http://dx.doi.org/10.1016/0025-3227(80)90051-1).

- Dan, G., Sultan, N., Savoye, B., Deverchere, J., Yelles, K., 2009. Quantifying the role of sandy-silty sediments in generating slope failures during earthquakes: example from the Algerian margin. *Int. J. Earth Sci.* 98, 769–789, <http://dx.doi.org/10.1007/s00531-008-0373-5>.
- Dennielou, B., Droz, L., Babonneau, N., Jacq, C., Bonnel, C., Picot, M., Le Saout, M., Saout, Y., Bez, M., Savoye, B., 2017. Morphology, structure, composition and build-up processes of the active channel-mouth lobe complex of the Congo deep-sea fan with inputs from remotely operated underwater vehicle (ROV) multibeam and video surveys. *Deep Sea Res. Part II Top. Stud. Oceanogr.* 142, 25–49.
- Dennielou, B., Huchon, A., Beaudouin, C., Berné, S., 2006. Vertical grain-size variability within a turbidite levee: autocyclicity or allocyclicity? A case study from the Rhône neofan, Gulf of Lions, Western Mediterranean. *Mar. Geol.* 234, 191–213, <http://dx.doi.org/10.1016/j.margeo.2006.09.019>.
- Dennielou, B., Jégou, I., Droz, L., Jouet, G., Cattaneo, A., Berné, S., Aslanian, D., Loubrieu, B., Rabineau, M., Bermell, S., 2019. Major modification of sediment routing by a large Mass Transport Deposit in the Gulf of Lions (Western Mediterranean). *Mar. Geol.* 411, 1–20, <http://dx.doi.org/10.1016/j.margeo.2019.01.011>.
- dos Reis, A.T., Gorini, C., Mauffret, A., 2005. Implications of salt-sediment interactions on the architecture of the Gulf of Lions deep-water sedimentary systems - Western Mediterranean Sea. *Mar. Pet. Geol.* 22, 713–746, <http://dx.doi.org/10.1016/j.marpetgeo.2005.03.006>.
- dos Reis, A.T., Gorini, C., Mauffret, A., Weibul, W.W., Mepen, M., Di Lello, M., Stratievsky, C., 2015. Radial Gliding Evinced by Subsalt Relief and Salt-related Structures: the Example of the Gulf of Lions. *Western Mediterranean*, <http://dx.doi.org/10.1101/sbf2005-191>.
- Droz, L., 2003. PROGRES cruise, RV Le Suroît., <http://dx.doi.org/10.17600/3020080>.
- Droz, L., 1983. L'éventail sous-marin profond du Rhône (Golfe du Lion): grands traits morphologiques et structure semi-profonde.
- Droz, L., Bellaiche, G., 1985. Rhone deep-sea fan: morphostructure and growth pattern. *Am. Assoc. Pet. Geol. Bull.* 69, 460–479.
- Droz, L., dos Reis, A.T., Rabineau, M., Berné, S., Bellaiche, G., 2006. Quaternary turbidite systems on the northern margins of the Balearic Basin (Western Mediterranean): a synthesis. *Geo-Marine Lett.* 26, 347–359, <http://dx.doi.org/10.1007/s00367-006-0044-0>.
- Droz, L., Kergoat, R., Cochonat, P., Berné, S., 2001. Recent sedimentary events in the western Gulf of Lions (Western Mediterranean). *Mar. Geol.* 176, 23–37, [http://dx.doi.org/10.1016/S0025-3227\(01\)00147-5](http://dx.doi.org/10.1016/S0025-3227(01)00147-5).
- Eckel, E.B. (Ed.), 1958. Highw. Res. Board Spec. Rep. 29, 232.
- Fanget, A.S., Bassetti, M.A., Arnaud, M., Chiffolleau, J.F., Cossa, D., Goineau, A., Fontanier, C., Buscail, R., Jouet, G., Maillet, G.M., Negri, A., Dennielou, B., Berné, S., 2013. Historical evolution and extreme climate events during the last 400 years on the Rhone prodelta (NW Mediterranean). *Mar. Geol.* 346, 375–391, <http://dx.doi.org/10.1016/j.margeo.2012.02.007>.
- Frey Martinez, J., Cartwright, J., Hall, B., 2005. 3D seismic interpretation of slump complexes: examples from the continental margin of Israel. *Basin Res.* 17, 83–108, <http://dx.doi.org/10.1111/j.1365-2117.2005.00255.x>.
- Frigola, J., Canals, M., Cacho, I., Moreno, A., Sierra, F.J., Flores, J.A., Berné, S., Jouet, G., Dennielou, B., Herrera, G., Pasqual, C., Grimalt, J.O., Galavazi, M., Schneider, R., 2012. A 500 kyr record of global sea-level oscillations in the Gulf of Lion, Mediterranean Sea: new insights into MIS 3 sea-level variability. *Clim. Past Discuss.* 8, 1067–1077, <http://dx.doi.org/10.5194/cpd-8-1067-2012>.
- Gamboa, D., Alves, T., Cartwright, J., 2011. Distribution and characterization of failed (mega)blocks along salt ridges, southeast Brazil: implications for vertical fluid flow on continental margins. *J. Geophys. Res.* 116, B08103, <http://dx.doi.org/10.1029/2011JB008357>.
- Gamboa, D., Alves, T.M., 2016. Bi-modal deformation styles in confined mass-transport deposits: examples from a salt minibasin in SE Brazil. *Mar. Geol.* 379, 176–193, <http://dx.doi.org/10.1016/j.margeo.2016.06.003>.
- Gawthorpe, R.L., Clemmey, H., 1985. Geometry of submarine slides in the Bowland Basin (Dinantian) and their relation to debris flows. *J. Geol. Soc.* 142, 555–565, <http://dx.doi.org/10.1144/gsjgs.142.3.0555>.
- Gee, M.J.R., Gawthorpe, R.L., Friedmann, S.J., 2006. Triggering and Evolution of a Giant Submarine Landslide, Offshore Angola, Revealed by 3D Seismic Stratigraphy and Geomorphology. *J. Sediment. Res. A Sediment. Petr. Process.* 76, 9–19, <http://dx.doi.org/10.2110/jsr.2006.02>.
- Hampton, M.A., Lee, H.J., Locat, J., 1996. Submarine landslides. *Rev. Geophys.* 34, 33–59, <http://dx.doi.org/10.1029/95RG03287>.
- Heidarzadeh, M., Muhamari, A., Wijanarto, A.B., 2018. Insights on the Source of the 28 September 2018 Sulawesi Tsunami, Indonesia Based on Spectral Analyses and Numerical Simulations. *Pure Appl. Geophys.*, 1–19, <http://dx.doi.org/10.1007/s00024-018-2065-9>.
- Hjelstuen, B.O., Sejrup, H.P., Halldason, H., Nygård, A., Berstad, I.M., Knorr, G., 2004. Late Quaternary seismic stratigraphy and geological development of the south Vøring margin, Norwegian Sea. *Quat. Sci. Rev.* 23, 1847–1865.
- Hsu, K.J., 1973. The origin of the Mediterranean evaporites. Initial reports Deep sea Drill. Proj. 13, 1203–1231.
- Hühnerbach, V., Masson, D.G., 2004. Landslides in the North Atlantic and its adjacent seas: an analysis of their morphology, setting and behaviour. *Mar. Geol.*, <http://dx.doi.org/10.1016/j.margeo.2004.10.013>.
- Jouet, G., 443 pp 2007. Enregistrements stratigraphiques des cycles climatiques et eustatiques du Quaternaire terminal - Modélisations de la marge continentale du Golfe du Lion. Univ. de Bretagne Occidentale, Brest, France.
- Jouet, G., Berné, S., Rabineau, M., Bassetti, M.A., Bernier, P., Dennielou, B., Sierra, F.J., Flores, J.A., Taviani, M., 2006. Shoreface migrations at the shelf edge and sea-level changes around the Last Glacial Maximum (Gulf of Lions, NW Mediterranean). *Mar. Geol.* 234, 21–42, <http://dx.doi.org/10.1016/j.margeo.2006.09.012>.
- Kettner, A.J., Syvitski, J.P.M., 2009. Fluvial responses to environmental perturbations in the Northern Mediterranean since the Last Glacial Maximum. *Quat. Sci. Rev.* 28, 2386–2397, <http://dx.doi.org/10.1016/j.quascirev.2009.05.003>.
- Kvalstad, T.J., Andresen, L., Forsberg, C.F., Berg, K., Bryn, P., Wangen, M., 2005. The Storegga slide: evaluation of triggering sources and slide mechanics. *Mar. Pet. Geol.* 22, 245–256, <http://dx.doi.org/10.1016/j.marpetgeo.2004.10.019>.
- Lambeck, K., Rouby, H., Purcell, A., Sun, Y., Sambridge, M., 2014. Sea level and global ice volumes from the Last Glacial Maximum to the Holocene. *Proc. Natl. Acad. Sci. U. S. A.* 111, 15296–15303, <http://dx.doi.org/10.1073/pnas.1411762111>.
- Lastras, G., 2007. Continental margin instability in the NW Mediterranean. *Geologica Acta*.
- Lastras, G., De Blasio, F.V., Canals, M., Elverhoi, A., 2005. Conceptual and numerical modeling of the BIG'95 debris flow, Western Mediterranean Sea. *J. Sediment. Res. A Sediment. Petr. Process.* 75, 784–797, <http://dx.doi.org/10.2110/jsr.2005.063>.
- Le Pichon, X., Pautot, G., Auzende, J.-M., Olivet, J.-L., 1971. La Méditerranée occidentale depuis l'Oligocène Schema d'évolution. *Earth Planet. Sci. Lett.* 13, 145–152, [http://dx.doi.org/10.1016/0012-821X\(71\)90117-8](http://dx.doi.org/10.1016/0012-821X(71)90117-8).
- Lee, H.J., 2009. Timing of occurrence of large submarine landslides on the Atlantic Ocean margin. *Mar. Geol.* 264, 53–64, <http://dx.doi.org/10.1016/j.margeo.2008.09.009>.
- Leroux, E., Rabineau, M., Aslanian, D., Granjeon, D., Droz, L., Gorini, C., 2014. Stratigraphic simulations of the shelf of the Gulf of Lions: testing subsidence rates and sea-level curves during the Pliocene and Quaternary. *Terra Nov.* 26, 230–238, <http://dx.doi.org/10.1111/ter.12091>.
- Leroux, E., Aslanian, D., Rabineau, M., Moulin, M., Granjeon, D., Gorini, C., Droz, L., 2015. Sedimentary markers in the Provençal Basin (Western Mediterranean): a window into deep geodynamic processes. *Terra Nov.* 27, 122–129, <http://dx.doi.org/10.1111/ter.12139>.
- Leynaud, D., Mienert, J., Vanneste, M., 2009. Submarine mass movements on glaciated and non-glaciated European continental margins: a review of triggering mechanisms and preconditions to failure. *Mar. Pet. Geol.* 26, 618–632, <http://dx.doi.org/10.1016/j.marpetgeo.2008.02.008>.
- Leynaud, D., Sultan, N., Mienert, J., 2007. The role of sedimentation rate and permeability in the slope stability of the formerly glaciated Norwegian continental margin: the Storegga slide model. *Landslides* 4, 297–309, <http://dx.doi.org/10.1007/s10346-007-0086-z>.
- Li, W., Alves, T.M., Urlaub, M., Georgioupolou, A., Klaucke, I., Wynn, R.B., Gross, F., Meyer, M., Repschläger, J., Berndt, C., Krastel, S., 2017. Morphology, age and sediment dynamics of the upper headwall of the Sahara Slide Complex, Northwest Africa: evidence for a large Late Holocene failure. *Mar. Geol.* 393, 109–123, <http://dx.doi.org/10.1016/j.margeo.2016.11.013>.
- Locat, J., Lee, H.J., 2002. Submarine landslides: advances and challenges. *Can. Geotech. J.* 39, 193–212, <http://dx.doi.org/10.1139/t01-089>.
- Locat, J., Leroueil, S., Locat, A., Lee, H., 2014. Weak Layers: Their Definition and Classification from a Geotechnical Perspective. Springer, Cham, pp. 3–12, http://dx.doi.org/10.1007/978-3-319-00972-8_1.
- Lofi, J., Rabineau, M., Gorini, C., Berne, S., Clauzon, G., De Clarens, P., Tadeu Dos Reis, A., Mountain, G.S., Ryan, W.B.F., Steckler, M.S., Fouquet, C., 2003. Plio-Quaternary prograding clinoform wedges of the western Gulf of Lion continental margin (NW Mediterranean) after the Messinian Salinity Crisis. *Mar. Geol.* 198, 289–317, [http://dx.doi.org/10.1016/S0025-3227\(03\)00120-8](http://dx.doi.org/10.1016/S0025-3227(03)00120-8).
- Lombo Tombo, S., Dennielou, B., Berné, S., Bassetti, M.A., Toucanne, S., Jorry, S.J., Jouet, G., Fontanier, C., 2015. Sea-level control on turbidite activity in the Rhone canyon and the upper fan during the Last Glacial Maximum and Early deglacial. *Sediment. Geol.*, <http://dx.doi.org/10.1016/j.sedgeo.2015.04.009>.
- Loubrieu, B., 1997. CALMAR97 cruise, RV L'Atalante., <http://dx.doi.org/10.17600/97010120>.
- Loutit, T.S., Hardenbol, J., Vail, P.R., Baum, G.R., 1988. Condensed sections: the key to age determination and correlation of continental margin sequences, in: sea-Level Changes. SEPM (Society for Sedimentary Geology), 183–213, <http://dx.doi.org/10.2110/pec.88.01.0183>.
- Masson, D., Harbitz, C., Wynn, R., Pedersen, G., Løvholt, F., 2006. Submarine landslides: processes, triggers and hazard prediction. *Philos. Trans. R. Soc. A Math. Phys. Eng. Sci.* 364, 2009–2039, <http://dx.doi.org/10.1098/rsta.2006.1810>.
- McAdoo, B.G., Pratson, L.F., Orange, D.L., 2000. Submarine landslide geomorphology, US continental slope. *Mar. Geol.*, [http://dx.doi.org/10.1016/S0025-3227\(00\)00050-5](http://dx.doi.org/10.1016/S0025-3227(00)00050-5).
- Micallef, A., Masson, D.G., Berndt, C., Stow, D.A.V., 2007. Morphology and mechanics of submarine spreading: a case study from the Storegga Slide. *J. Geophys. Res. Earth Surf.*, <http://dx.doi.org/10.1029/2006JF000739>.
- Moscadelli, L., Wood, L., 2008. New classification system for mass transport complexes in offshore Trinidad. *Basin Res.* 20, 73–98, <http://dx.doi.org/10.1111/j.1365-2117.2007.00340.x>.
- Nissen, S.E., Haskell, N.L., Steiner, C.T., Coterill, K.L., 1999. Debris flow outrunner blocks, glide tracks, and pressure ridges identified on the Nigerian continental slope using 3-D seismic coherency. *Proc. Int. Conf. Lead. Edge Manuf.* 21st Century Lem21 18, 595–599, <http://dx.doi.org/10.1190/1.1438343>.
- Owen, M., Day, S., Maslin, M., 2007. Late Pleistocene submarine mass movements: occurrence and causes. *Quat. Sci. Rev.* 26, 958–978, <http://dx.doi.org/10.1016/j.quascirev.2006.12.011>.
- Peña, L.D., Goldstein, S.L., 2014. Thermohaline circulation crisis and impacts during the mid-Pleistocene transition. *Science* 345, 318–322, <http://dx.doi.org/10.1126/science.1249770>.
- Pirmez, C., Hiscott, R.N., Kronen, J.D., 1997. Sandy turbidite successions at the base of channel-levee systems of the Amazon Fan revealed by fms logs and cores:

- unraveling the facies architecture of large submarine fans. *Proc. Ocean Drill. Prog. Sci. Results.*
- Pope, E.L., Talling, P.J., Urlaub, M., Hunt, J.E., Clare, M.A., Challenor, P., 2015. Are large submarine landslides temporally random or do uncertainties in available age constraints make it impossible to tell? *Mar. Geol.* 369, 19–33, <http://dx.doi.org/10.1016/j.margeo.2015.07.002>.
- Posamentier, H.W., Kolla, V., 2003. Seismic geomorphology and stratigraphy of depositional elements in deep-water settings. *J. Sediment. Res. A Sediment. Petrol. Process.* 73, 367–388, <http://dx.doi.org/10.1306/11302730367>.
- Rabineau, M., Aslanian, D., 2007. SEEPGOL cruise, RV Le Suroît, <http://dx.doi.org/10.17600/7020080>.
- Rabineau, M., Berné, S., Aslanian, D., Olivet, J.-L., Joseph, P., Guillocheau, F., Bourillet, J.-F.F., Ledrezen, E., Granjeon, D., 2005. Sedimentary sequences in the Gulf of Lion: a record of 100,000 years climatic cycles. *Mar. Pet. Geol.* 22, 775–804, <http://dx.doi.org/10.1016/j.marpetgeo.2005.03.010>.
- Rabineau, M., Berné, S., Ledrezen, É., Lericolais, G., Marsset, T., Rotunno, M., 1998. 3D architecture of lowstand and transgressive Quaternary sand bodies on the outer shelf of the Gulf of Lion, France. *Mar. Pet. Geol.* 15, 439–452, [http://dx.doi.org/10.1016/S0264-8172\(98\)00015-4](http://dx.doi.org/10.1016/S0264-8172(98)00015-4).
- Rabineau, M., Berné, S., Olivet, J.-L., Aslanian, D., Guillocheau, F., Joseph, P., 2006. Paleo sea levels reconsidered from direct observation of paleoshoreline position during Glacial Maxima (for the last 500,000 yr). *Earth Planet. Sci. Lett.* 252, 119–137, <http://dx.doi.org/10.1016/j.epsl.2006.09.033>.
- Rabineau, M., Droz, L., Aslanian, D., 2013. AM-MED-1 cruise, RV Le Suroît, <http://dx.doi.org/10.17600/1800821>.
- Rabineau, M., Leroux, E., Aslanian, D., Bache, F., Gorini, C., Moulin, M., Molliex, S., Droz, L., dos Reis, A.T., Rubino, J.L., Guillocheau, F., Olivet, J.L., 2014. Quantifying subsidence and isostatic readjustment using sedimentary paleomarkers, example from the Gulf of Lion. *Earth Planet. Sci. Lett.* 388, 353–366, <http://dx.doi.org/10.1016/j.epsl.2013.11.059>.
- Rebouille, C., Olu, K., Baudin, F., Khrapounoff, A., Dennielou, B., Arnaud-Haond, S., Babonneau, N., Bayle, C., Beckler, J., Bessette, S., Bomblet, B., Bourgeois, S., Brandly, C., Caprais, J.C., Cathalot, C., Charlier, K., Corvaisier, R., Croguennec, C., Cruaud, P., Decker, C., Droz, L., Gayet, N., Godfroy, A., Hourdez, S., Le Bruchec, J., Saout, J., Le Saout, M., Lesongeur, F., Martinez, P., Mejanelle, L., Michalopoulos, P., Mouchel, O., Noel, P., Pastor, L., Picot, M., Pignet, P., Pozzato, L., Pruski, A.M., Rabiller, M., Raimonet, M., Ragueneau, O., Reysse, J.L., Rodier, P., Ruesch, B., Ruffine, L., Savignac, F., Senyarchic, C., Schnyder, J., Sen, A., Stetten, E., Sun, M.Y., Taillefert, M., Teixeira, S., Tisnerat-Labordé, N., Toffin, L., Tourolle, J., Toussaint, F., Vétion, G., Jouanneau, J.M., Bez, M., 2017. The Congolobe project, a multidisciplinary study of Congo deep-sea fan lobe complex: overview of methods, strategies, observations and sampling. *Deep Sea Res. Part II Top. Stud. Oceanogr.* 142, 7–24, <http://dx.doi.org/10.1016/j.dsro.2016.05.006>.
- Reimer, P.J., Edouard Bard, B., Alex Bayliss, B., Warren Beck, B.J., Paul Blackwell, B.G., Christopher Bronk Ramsey, B., 2013. *IntCal13 and Marine13 radiocarbon age calibration curves 0–50,000 years cal bp*. *Radiocarbon* 55, 1869–1887.
- Riboulot, V., Thomas, Y., Berné, S., Jouet, G., Cattaneo, A., 2014. Control of Quaternary sea-level changes on gas seeps. *Geophys. Res. Lett.* 41, 4970–4977, <http://dx.doi.org/10.1002/2014GL060460>.
- Ridente, D., Trincardi, F., Piva, A., Asioli, A., 2009. The combined effect of sea level and supply during Milankovitch cyclicity: Evidence from shallow-marine δ¹⁸O records and sequence architecture (Adriatic margin). *Geology* 37, 1003–1006, <http://dx.doi.org/10.1130/G25730A.1>.
- Rothwell, R.G., Thomson, J., Kähler, G., 1998. Low-sea-level emplacement of a very large Late Pleistocene 'megaturbidite' in the Western Mediterranean Sea. *Nature* 392, 377–380, <http://dx.doi.org/10.1038/32871>.
- Roveri, M., Lugli, S., Manzi, V., Schreiber, B.C., 2008. The Messinian Sicilian stratigraphy revisited: new insights for the Messinian salinity crisis. *Terra Nov.* 20, 483–488, <http://dx.doi.org/10.1111/j.1365-3121.2008.00842.x>.
- Sassa, S., Takagawa, T., 2019. Liquefied gravity flow-induced tsunami: first evidence and comparison from the 2018 Indonesia Sulawesi earthquake and tsunami disasters. *Landslides* 16, 195–200, <http://dx.doi.org/10.1007/s10346-018-1114-x>.
- Sawyer, D.E., Flemings, P.B., Dugan, B., Germaine, J.T., 2009. Retrogressive failures recorded in mass transport deposits in the Ursa Basin. Northern Gulf of Mexico, <http://dx.doi.org/10.1029/2008JB006159>, 114.
- Sawyer, D.E., Hodelka, B., 2016. Tiny Fossils, Big Impact: The Role of Foraminifera-Enriched Condensed Section in Arresting the Movement of a Large Retrogressive Submarine Landslide in the Gulf of Mexico. Springer, Cham, pp. 479–486, http://dx.doi.org/10.1007/978-3-319-20979-1_48.
- Schuster, R.L., Krizek, R.J., 1978. *Landslides analysis and control*. Washington Transportation Research Board, special report 176. Natl. Acad. Sci. WA 234.
- Séranne, M., 1999. *The Gulf of Lion continental margin (NW Mediterranean) revisited by IBS: an overview*. *Geol. Soc. London, Spec. Publ.* 156, 15–36.
- Shipp, R.C., Nott, J.A., Newlin, J.A., 2004. Physical characteristics and impact of mass transport complexes on deepwater jetted conductors and suction anchor piles. In: Offshore Technology Conference, Offshore Technology Conference, <http://dx.doi.org/10.4043/16751-MS>.
- Sierro, F.J., Andersen, N., Bassetti, M.A., Berné, S., Canals, M., Curtis, J.H., Dennielou, B., Flores, J.A., Frigola, J., Gonzalez-Mora, B., Grimalt, J.O., Hodell, D.A., Jouet, G., Pérez-Folgado, M., Schneider, R., 2009. Phase relationship between sea level and abrupt climate change. *Quat. Sci. Rev.* 28, 2867–2881, <http://dx.doi.org/10.1016/j.quascirev.2009.07.019>.
- Solow, A.R., Chatyor, J.D., ten Brink, U.S., Solow, A.R., Andrews, B.D., Chatyor, J.D., ten Brink, U.S., Solow, A.R., Andrews, B.D., 2009. Size distribution of submarine landslides along the U.S. Atlantic margin. *Mar. Geol.* 264, 16–27, <http://dx.doi.org/10.1016/j.margeo.2008.08.007>.
- Steckler, M.S., Watts, A.B., 1980. The Gulf of Lion: subsidence of a young continental margin. *Nature* 287, 425–429, <http://dx.doi.org/10.1038/287425a0>.
- Stoecklin, A., Friedli, B., Puzrin, A.M., 2017. Sedimentation as a control for large submarine landslides: mechanical modeling and analysis of the Santa Barbara Basin. *J. Geophys. Res. Solid Earth* 122, 8645–8663, <http://dx.doi.org/10.1002/2017JB014752>.
- Stuiver, M., Reimer, P.J., Reimer, R.W., [www program] 2017. *Calib 7.1*.
- Sultan, N., Cochonat, P., Canals, M., Cattaneo, A., Dennielou, B., Haflidason, H., Laberg, J.S., Long, D., Mienert, J., Trincardi, F., Urgeles, R., Vorren, T.O., Wilson, C., 2004. Triggering mechanisms of slope instability processes and sediment failures on continental margins: a geotechnical approach. *Mar. Geol.* 213, 291–321, <http://dx.doi.org/10.1016/j.margeo.2004.10.011>.
- Sultan, N., Gaudin, M., Berne, S., Canals, M.M., Urgeles, R., Lafuerza, S., 2007. Analysis of slope failures in submarine canyon heads: an example from the Gulf of Lions. *J. Geophys. Res. Earth Surf.* 112, F01009, <http://dx.doi.org/10.1029/2005JF000408>.
- Sultan, N., Voisset, M., 2002. GMO2 - CARNAC Cruise, RV Le Suroît, <http://dx.doi.org/10.17600/2020080>.
- Tappin, D.R., Matsumoto, T., Watts, P., Satake, K., McMurry, G.M., Matsuyama, M., Lafoy, Y., Tsuji, Y., Kanamatsu, T., Lus, W., Iwabuchi, Y., Yeh, H., Matsumoto, Y., Nakamura, M., Mahoi, M., Hill, P., Crook, K., Anton, L., Walsh, J.P., 1999. Sediment slump likely caused 1998 Papua New Guinea tsunami. *Eos, Trans. Am. Geophys. Union* 80, 329, <http://dx.doi.org/10.1029/99EO00241>.
- ten Brink, U.S.S., Barkan, R., Andrews, B.D.D., Chatyor, J.D.D., 2009. *Size distributions and failure initiation of submarine and subaerial landslides*. *Earth Planet. Sci. Lett.* 287, 31–42.
- Tesson, M., Gensous, B., 1998. L'enregistrement des cycles climatiques et eustatiques quaternaires de marges récentes du bassin Nord-Méditerranéen. *Comptes Rendus l'Académie des Sci. - Ser. IIA - Earth Planet. Sci.* 326, 121–127, [http://dx.doi.org/10.1016/S1251-8050\(97\)87456-3](http://dx.doi.org/10.1016/S1251-8050(97)87456-3).
- Torres, J., Savoye, B., Cochonat, P., 1995. The Effects of Late Quaternary Sea-level Changes on the Rhone Slope Sedimentation (Northwestern Mediterranean), as Indicated by Seismic Stratigraphy. *SEPM J. Sediment. Res.* 65B, 368–387, <http://dx.doi.org/10.1306/D4268257-2B26-11D7-8648000102C1865D>.
- Torres, J., Droz, L., Savoye, B., Terentieva, E., Cochonat, P., Kenyon, N.H., Canals, M., 1997. Deep-sea avulsion and morphosedimentary evolution of the Rhône Fan Valley and Neofan during the Late Quaternary (North-Western Mediterranean Sea). *Sedimentology* 44, 457–477, <http://dx.doi.org/10.1046/j.1365-3091.1997.d0136.x>.
- Toucanne, S., Angue Minto'o, C.M., Fontanier, C., Bassetti, M.-A., Jorry, S.J., Jouet, G., 2015. Tracking rainfall in the northern Mediterranean borderlands during sapropel deposition. *Quat. Sci. Rev.* 129, 178–195, <http://dx.doi.org/10.1016/j.quascirev.2015.10.016>.
- Trincardi, F., Argani, A., 1990. Gela submarine slide: a major basin-wide event in the plio-quaternary foredeep of Sicily. *Geo-Marine Lett.* 10, 13–21, <http://dx.doi.org/10.1007/BF02431017>.
- Urgeles, R., Camerlenghi, A., 2013. Submarine landslides of the Mediterranean Sea: trigger mechanisms, dynamics, and frequency-magnitude distribution. *J. Geophys. Res. Earth Surf.* <http://dx.doi.org/10.1029/2013JF002720>.
- Urlaub, M., Geersen, J., Krastel, S., Schwenk, T., 2018. Diatom ooze: Crucial for the generation of submarine mega-slides? *Geology* 46, 2–5, <http://dx.doi.org/10.1130/C39892.1>.
- Urlaub, M., Talling, P.J., Masson, D.G., 2013. Timing and frequency of large submarine landslides: implications for understanding triggers and future geohazard. *Quat. Sci. Rev.* 72, 63–82, <http://dx.doi.org/10.1016/j.quascirev.2013.04.020>.
- Urlaub, M., Talling, P.J., Zervos, A., Masson, D., 2015. What causes large submarine landslides on low gradient (<2°) continental slopes with slow (~0.15 m/kyr) sediment accumulation? *J. Geophys. Res. Solid Earth* 120, 6722–6739, <http://dx.doi.org/10.1002/2015JB012347>.
- Vanneste, M., Forsberg, C.F., Glimsdal, S., Harbitz, C.B., Issler, D., Kvalstad, T.J., Løvholt, F., Nadim, F., 2013. Submarine landslides and their consequences: what Do We know, what can We Do? In: *Landslide Science and Practice*. Springer, Berlin Heidelberg, Berlin, Heidelberg, pp. 5–17, http://dx.doi.org/10.1007/978-3-642-31427-8_1.
- Zhou, L., Liu, J., Saito, Y., Gao, M., Diao, S., Qiu, J., Pei, S., 2016. Modern sediment characteristics and accumulation rates from the delta front to prodelta of the Yellow River (Huanghe). *Geo-Marine Lett.* 36, 247–258.